

# Oligoclonal tumor-specific CD8 T-cell revival and IRE1 $\alpha$ /XBPI-GDF15-mediated immunosuppressive niches determine neoadjuvant chemoimmunotherapy efficacy in cervical cancer

Guangxu Cao,<sup>1</sup> Yuhuan Wang ,<sup>1</sup> Huimin Zeng,<sup>2</sup> Yong Zhi,<sup>3</sup> Yi Guo,<sup>1</sup> Mengting Xu,<sup>1</sup> Yetian Ruan,<sup>1</sup> Ying Wang,<sup>1</sup> Yuhang Xiao,<sup>1</sup> Jianqiao Lu,<sup>1</sup> Ka Yu Tse,<sup>4</sup> Jinli Gao,<sup>5</sup> Qingfeng Zhang,<sup>6</sup> Chenfei Wang ,<sup>7</sup> Zhiqiang Han,<sup>2,8</sup> Fang Li 

**To cite:** Cao G, Wang Y, Zeng H, et al. Oligoclonal tumor-specific CD8 T-cell revival and IRE1 $\alpha$ /XBPI-GDF15-mediated immunosuppressive niches determine neoadjuvant chemoimmunotherapy efficacy in cervical cancer. *Journal for ImmunoTherapy of Cancer* 2025;13:e012630. doi:10.1136/jitc-2025-012630

► Additional supplemental material is published online only. To view, please visit the journal online (<https://doi.org/10.1136/jitc-2025-012630>).

GC, YW, HZ and YZ contributed equally.

Accepted 28 October 2025

## ABSTRACT

**Background** Neoadjuvant chemoimmunotherapy (NACI) shows promise for locally advanced cervical cancer (LACC), but drug-tolerant persister (DTP) cells and immunosuppressive microenvironmental adaptations limit clinical efficacy. The underlying determinants governing heterogeneous responses to NACI regimens remain poorly understood, particularly regarding how dynamic tumor-immune interactions shape therapeutic outcomes.

**Methods** We characterized microenvironmental dynamics in patients with LACC by integrating single-cell RNA sequencing (RNA-seq), single-cell VDJ sequencing (n=10, five paired pre-NACI/post-NACI samples) and spatial transcriptomics (ChiCTR2300072535). Pathological response was assessed using major pathological response criteria. The findings were validated in an independent NACI cohort (n=23 with RNA-seq), multiplex immunohistochemistry (mIHC) analysis of six surgically resected specimens, as well as functional in vitro and murine models.

**Results** MPR patients exhibited cytotoxic revival via oligoclonal expansion of tumor-reactive CD8+T cell clones and CCR5-mediated myeloid-T cell crosstalk. Conversely, non-MPR tumors exhibited endoplasmic reticulum (ER) stress-adapted DTP cells with elevated ER stress signaling, accompanied by a deficiency in tumor-specific T-cell clone expansion and an accumulation of transforming growth factor beta receptor 2 (TGFRB2) + myeloid DTP niches. Mechanistically, ER stress signaling via the inositol-requiring enzyme 1 alpha (IRE1 $\alpha$ ) / X-box binding protein 1 (XBPI) axis induces growth differentiation factor 15 (GDF15) production in DTP cells, contributing to treatment-resistant microdomains. Pharmacological IRE1 $\alpha$  inhibition synergized with chemoimmunotherapy to eradicate DTP populations in murine models.

**Conclusions** This study provides critical insights that NACI resistance stems from adaptive ER stress signaling in DTP cells and spatially organized immunosuppressive networks. Targeting the IRE1 $\alpha$ /XBPI-GDF15 axis represents an actionable strategy to reprogram microenvironmental ecology and improve immunotherapy outcomes.

## BACKGROUND

Immunotherapy has revolutionized the non-surgical management of cervical cancer (CC). Clinical trials have validated the efficacy and safety of multiple immune checkpoint inhibitor (ICI)-based regimens, including combinations with chemotherapy<sup>1–4</sup> and chemoradiotherapy,<sup>5</sup> in advanced or metastatic CC. Building on this foundation, Li *et al.* recently demonstrated the potential of neoadjuvant chemoimmunotherapy (NACI) using camrelizumab, an anti-programmed cell death protein 1 (PD-1) antibody, with cisplatin plus nab-paclitaxel for locally advanced CC (LACC), achieving an unprecedented objective response rate.<sup>6</sup> Despite these advances, the modest complete response rate underscores persistent knowledge gaps in how combinatorial therapies remodel the tumor microenvironment (TME) to drive complete eradication. Critically, overcoming drug-tolerant persister (DTP) cells and their associated immunosuppressive microenvironmental adaptations represents a fundamental prerequisite for optimizing therapeutic outcomes.

Single-cell profiling studies across malignancies—including lung,<sup>7–8</sup> breast,<sup>9–10</sup> colorectal,<sup>11–12</sup> renal,<sup>13</sup> and head/neck<sup>14</sup> cancers—have delineated how ICIs remodel the tumor ecosystem. Emerging evidence indicates that immunotherapy efficacy is mediated by clonal expansion and functional reinvigoration of tumor-specific CD8+T cells. Progenitor exhausted T cells (Tpex) and tissue-resident memory T cells (Trm), which serve as cellular reservoirs for sustaining antitumor immunity,<sup>15–16</sup> are critical to this process. Conversely,



© Author(s) (or their employer(s)) 2025. Re-use permitted under CC BY-NC. No commercial re-use. See rights and permissions. Published by BMJ Group.

For numbered affiliations see end of article.

**Correspondence to**  
Professor Fang Li;  
[fang\\_li@tongji.edu.cn](mailto:fang_li@tongji.edu.cn)

Professor Zhiqiang Han;  
[hanzq2003@126.com](mailto:hanzq2003@126.com)

Professor Chenfei Wang;  
[08chenfeiwang@tongji.edu.cn](mailto:08chenfeiwang@tongji.edu.cn)



## WHAT IS ALREADY KNOWN ON THIS TOPIC

Locally advanced cervical cancer (LACC) accounts for 37% of newly diagnosed cases globally, with higher prevalence in resource-limited regions. A recent phase II trial demonstrates neoadjuvant chemoimmunotherapy (NACI) achieves 98% objective response rates, yet only 19% attain complete pathological remission, suggesting unresolved resistance mechanisms. No prior studies have decoded the spatiotemporal evolution of LACC microenvironments during NACI.

## WHAT THIS STUDY ADDS

We identified clonally expanded CD8+Tcell populations in major pathological response patients exhibiting a cytotoxic tissue-resident memory (Trm) phenotype, alongside proliferative T-cell receptor (TCR) clonotypes targeting tumor neoantigens. Importantly, we uncovered a novel immunosuppressive axis mediated by drug-tolerant persister (DTP) cells and further verified by *in vitro* and *in vivo* experiments: inositol-requiring enzyme 1 alpha (IRE1 $\alpha$ ) / X-box binding protein 1 (XBP1) axis-driven growth differentiation factor 15 (GDF15) secretion activated transforming growth factor beta receptor 2 (TGFBR2) signaling in myeloid cells, thereby establishing an immunosuppressive niche. This mechanism provides the first functional link between stress responses and adaptive immune evasion in NACI resistance.

## HOW THIS STUDY MIGHT AFFECT RESEARCH, PRACTICE OR POLICY

Our findings advance LACC treatment by bridging mechanistic insights to clinical translation through two key applications. First, targeting the IRE1 $\alpha$ /XBP1 signaling or GDF-15 blockade synergizes with NACI to overcome resistance. Second, analysis of dominant CD8+TCR clonotypes associated with complete remission reveals dual clinical opportunities. These tumor-specific T cells provide actionable TCR sequences for personalized adoptive therapies in refractory patients, while tissue-resident memory T cell (Trm) signatures offer prognostic biomarkers.

other components, such as interleukin-1 beta (IL1B) + monocytes and C-C motif chemokine ligand 2 (CCL2) + cancer-associated fibroblasts, can subvert ICI efficacy by impairing T-cell functionality.<sup>12 17</sup> Notably, the majority of studies have focused on immune/stromal drivers of response resistance, while the biology of persistent tumor cells remains poorly characterized.

Investigating the mechanisms underlying tumor cell persistence during immunotherapy and identifying their vulnerabilities are crucial for developing strategies to improve immunotherapy outcomes.<sup>18</sup> Preclinical models of programmed cell death protein 1 (PD-1) antibody treatment have revealed that DTP cells exploit survival pathways such as tumor necrosis factor (TNF) and nuclear factor-kappa B (NF- $\kappa$ B) signaling<sup>19</sup> and actively remodel the TME through myeloid-derived suppressor cell (MDSC) recruitment<sup>20</sup> or prostaglandin-mediated T-cell suppression.<sup>21 22</sup> However, whether CC persister cells employ analogous strategies remains unknown.

The spatial architecture of tumors has emerged as a critical determinant of immunotherapy efficacy, with pretreatment spatial features serving as predictive

biomarkers for the ICI response.<sup>23–25</sup> However, the spatial ecology of CC, particularly in the context of NACI, remains inadequately understood. This study used an integrative multi-omics strategy combining longitudinal single-cell RNA sequencing (scRNA-seq), single-cell T-cell receptor sequencing (scTCR-seq), and spatial transcriptomics (ST), which enabled systematic dissection of TME remodeling during NACI. This study linked the MPR to the cytotoxic revival of hyperexpanded CD8+T cell clones during NACI. Conversely, some responders retained ER stress-featured DTP subpopulations that recruited MDSCs via serum amyloid A1 (SAA1) and growth differentiation factor 15 (GDF15) secretion, which further formed transforming growth factor beta receptor 2 (TGFBR2)+myeloid DTP niches. In addition, pre-existing mast cells suppressed antitumor immunity through prostaglandin pathways. These findings not only elucidate the mechanisms of post-NACI tumor persistence but also provide a blueprint for overcoming residual disease through targeted TME reprogramming.

## RESULTS

### Single-cell and spatial transcriptomic expression data revealed consistent cell compositions

While NACI has demonstrated clinical efficacy in LACC,<sup>1 6</sup> the mechanistic drivers of heterogeneous treatment responses remain poorly defined. To address this, we conducted multimodal profiling of seven patients with LACC who underwent NACI, with longitudinal tumor sampling before treatment and after the first therapy cycle for single-cell RNA/T-cell receptor (TCR) sequencing, complemented by spatial transcriptomics of postsurgical samples. Pathological assessment (online supplemental figure S1A) classified lesions as major pathological response (MPR; <10% viable tumor, n=2), non-MPR (NMPR; 20–50% viable tumor, n=5), or non-response (NR; n=1, Patient 6).<sup>26</sup> For Patient 2, MRI-based evaluation was unable to detect a pathological response. The clinicopathological characteristics and treatment timelines are detailed in online supplemental table S1 and figure S1B.

Following rigorous quality control, we established a single-cell transcriptomic atlas comprising 74,195 cells across major lineages, including T/natural killer (NK) cells, B/plasma cells, myeloid cells, epithelial cells, endothelial cells, and fibroblasts (figure 1B), with canonical marker confirmation (online supplemental figure S1D). While the baseline cellular compositions remained broadly consistent across patients (online supplemental figure S1C), NACI triggered dynamic shifts: epithelial cell depletion and fibroblast expansion (figure 1C), indicative of tumor elimination and fibrotic remodeling.<sup>27</sup>

Although the sample size was not statistically significant, the MPR sample presented an undetectable proportion of epithelial cells coupled with increased myeloid infiltration compared with the NMPR samples, indicating that myeloid engagement is involved in therapeutic efficacy

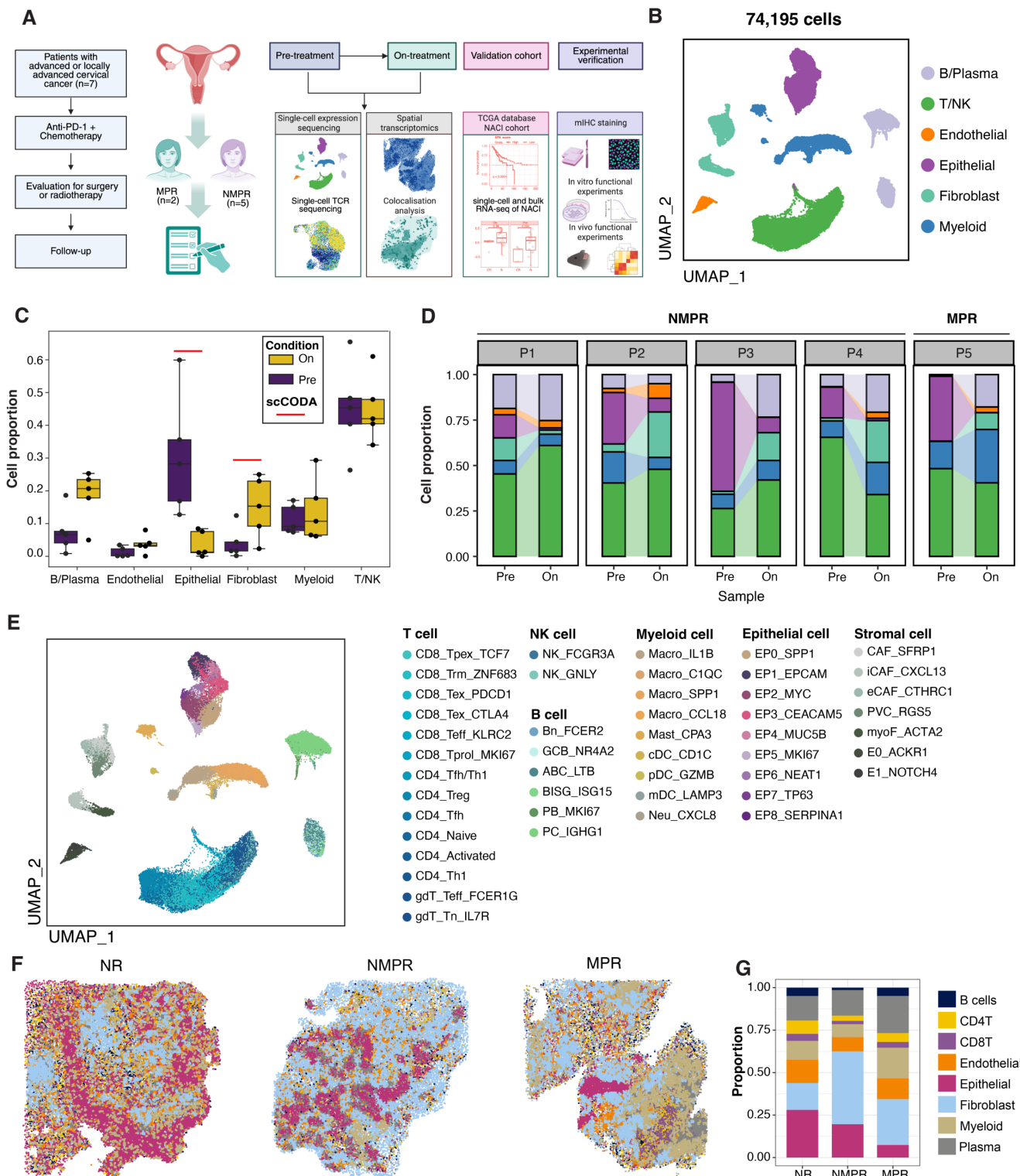


**Figure 1** Global analysis of the tumor microenvironment remodeled by neoadjuvant chemotherapy plus immunotherapy. (A) Schematic of the study design. (B) UMAP plot of the major cell types (denoted by colors). The cells were collected from five patients with cervical cancer. (C) Boxplots showing the changes in the proportion of each cell type before and after treatment. Statistical significance was analyzed via scCODA, with red bars indicating credible and significant results. The boxplots display the median, upper quartile, and lower quartile. (D) Alterations in the cellular composition of MPR and NMPR patients after treatment. The cell cluster colors are shown in B. (E) UMAP plot of forty-seven subtypes (denoted by colors). (F) Spatial distribution of spots annotated by CytoTRACE. The colors indicate the cell types referred to in G. (G) Cellular composition shown as a fraction for each sample. miHC, multiplex immunohistochemistry; MPR, major pathological response; NACI, neoadjuvant chemoimmunotherapy; NK, natural killer; NMPR, non-MPR; PD-1, programmed cell death protein 1; RNA-seq, RNA sequencing; scCODA, a Bayesian model for compositional single-cell data analysis; TCGA, the cancer genome atlas program; TCR, T-cell receptor; UMAP, uniform manifold approximation and projection.

(figure 1D). In addition, subclustering of each major cell lineage identified 47 specific subsets on the basis of their unique expression profiles for further analyses (figure 1E and online supplemental table S2). We then analyzed three ST samples from NR, NMPR and MPR lesions via integration with scRNA-seq via CytoSPACE (figure 1F and online supplemental figure S1E). The ST data confirmed lineage-specific spatial distributions, particularly myeloid dominance and epithelial absence, in MPR lesions (figure 1G). Overall, we dissected the longitudinal micro-environment dynamics during NACI in CC and further investigated their spatial relevance.

### ICI-related alterations in CD8 T-cell exhaustion and differentiation status

Integrated analysis of the scRNA-seq and scTCR-seq datasets revealed 12,743 high-quality tumor-infiltrating CD8+T cells (figure 2A,B). Unsupervised clustering revealed six distinct subsets exhibiting progressive differentiation states, including three exhausted subsets forming a phenotypic continuum (figure 2C).

The CD8\_Tpex\_TCF7 subset displayed progenitor-exhausted features characterized by co-expression of the stemness regulator TCF7<sup>28 29</sup> and the progenitor markers CD28 and GPR183<sup>30</sup> coupled with elevated granzyme K (GZMK) expression, suggesting retained cytotoxic potential.<sup>31</sup> Transitioning along the differentiation axis, CD8\_Tex\_PDCD1 cells lose their stem-like properties but maintain the expression of GZMK and the tumor-specific T-cell marker CXCL13<sup>32</sup> while acquiring exhaustion-associated transcription factors (*TOX*, *BATF*, and *PRDM1*) and inhibitory receptors (*PDCD1*, *TIGIT*, and *HAVCR2*). Terminal differentiation culminated in CD8\_Tex\_CTL4 cells showing complete loss of effector molecules alongside heightened CTLA4 expression. Three additional subsets were annotated as NK-like effector cells expressing cytotoxic granules, Trm with ZNF683 expression, and proliferating cells with mitotic activity. This stratification aligns with established frameworks for tumor-infiltrating T-cell heterogeneity<sup>29 30 33</sup> (online supplemental figure S2A and table S3).

NACI treatment induced profound remodeling of CD8+T cell dynamics, characterized by preferential expansion of the progenitor-exhausted CD8\_Tpex\_TCF7 subset and a decrease in the terminal exhausted CD8\_Tex\_CTL4 subset (figure 2D). Differential gene expression analysis revealed the coordinated upregulation of the expression of the cytotoxic effector GZMK and stress marker genes (*HSPA1A* and *HSP90AA1*) in treated cells (online supplemental figure S2B), paralleling known immunotherapy-induced stress adaptation.<sup>33</sup> Enrichment analyses revealed the activation of integrated stress response pathways (online supplemental figure S2C). In particular, the CD8\_Trm\_ZNF683 and CD8\_Tex\_PDCD1 subpopulations, which have been linked to the ICI response and tumor killing ability, presented relatively elevated stress response T-cell scores (online supplemental figure S2A).

A striking divergence was observed between the MPR and NMPR cohorts: CD8 T cells in the MPR sample differentiated from CD8\_Tex\_TCF7 to CD8\_Tex\_PDCD1 with complete attrition of CD8\_Tex\_CTL4. This effect was accompanied by synergistic induction of the cytotoxic mediators *IFNG*, *NKG7*, and *GZMK* (online supplemental figure S2D). Scoring analyses confirmed enhanced cytotoxicity in the MPR sample with significant alleviation of exhaustion (online supplemental figure S2E). These results suggest that NACI induced a cytotoxic revival in the MPR sample.

### A well-defined differentiation trajectory evolving from tissue-resistant memory to exhausted T cells in the MPR sample

Integrative analysis of TCR clonality and pseudotime trajectories revealed distinct differentiation programs underlying the NACI response. T cells with identical complementarity-determining region 3 (CDR3) sequences of TCR $\alpha$  and TCR $\beta$  were defined as originating from the same clone. The MPR sample exhibited pronounced clonal expansion, with hyperexpanded clones (more than 100 cells per clone) constituting more than 60% of the total CD8+T cells, whereas no hyperexpanded clones were observed in the NMPR sample (online supplemental figure S2F). Tumor specificity scoring demonstrated progressive coupling between clonal expansion and exhaustion progression,<sup>16</sup> where expanded clones accumulated both tumor reactivity signatures and terminal exhaustion markers (figure 2G).

Pseudotime reconstruction via RNA velocity (online supplemental figure S3A,B) and Slingshot delineated three differentiation axes: Lineage 1 (Tex\_PDCD1 to Tex\_CTL4) captured the progressive exhaustion of clonal progenitors, whereas Lineage 2 (Trm\_ZNF683 to Tex\_PDCD1) revealed tissue-resident memory contributions to the exhausted pool. Strikingly, the majority of MPR-derived T cells populated the terminal branches of lineages 1 and 2, with hyperexpanded clones preferentially localizing to late-exhaustion states. Conversely, NMPR T cells predominantly occupied Lineage 3 (CD8\_Tpex\_TCF7 to NK-like effectors) and early pseudotime phases (figure 2H). Furthermore, CD8+T cells in lineage 1 exhibited the highest tumor-specific scores (online supplemental figure S3C), with these scores showing a marked increase along the pseudotime progression of this lineage. These findings suggest that the TCR neoantigen recognition capacity determines differentiation fate selection, as productive engagement drives clones through exhaustion-associated trajectories (lineages 1 and 2), whereas limited antigen sensing defaults to alternative differentiation (lineage 3). The absence of Lineage 1 progression in NMPR samples implicates defective TCR-tumor ecosystem interactions as a barrier to the therapeutic response.

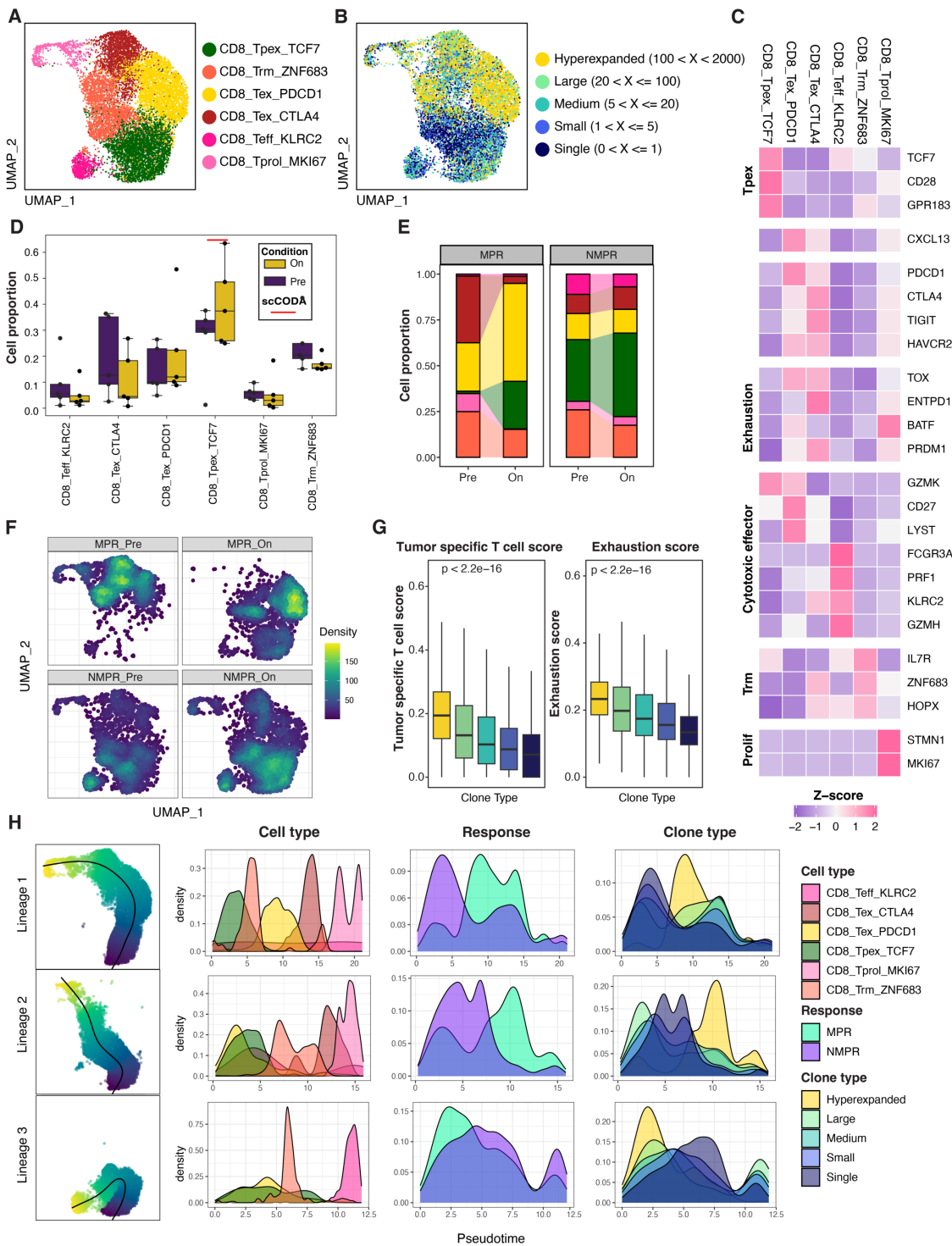


**Figure 2** CD8+Tcell exhaustion and hyperexpansion are enriched in MPR samples. (A) UMAP plot of CD8+T cell subsets (denoted by colors). (B) UMAP plot of CD8 T-cell clone size. The color indicates the size of the T-cell clone. (C) Heatmap showing marker genes of each T-cell cluster. (D) Boxplots showing the changes in the proportion of each CD8+T cell subset before and after treatment. Statistical significance was analyzed via scCODA, with red bars indicating credible and significant results. The boxplots display the median, upper quartile, and lower quartile. (E) Alterations in the cellular composition of MPR and NMPR patients after treatment. The cell cluster colors are shown in figure 3A. (F) UMAP plot of CD8+Tcell distribution. The color indicates the density of the CD8+T cells. (G) Boxplots showing the tumor-specific scores (left panel) and exhaustion scores of T cells with different clone sizes. Statistical significance was analyzed via the Kruskal-Wallis test. The boxplots display the median, upper quartile, and lower quartile. (H) The differentiated trajectory of CD8+T cells inferred via Slingshot. The UMAP plot displays the predicted lineages, comprising three trajectories (illustrated in the left panel). The density plot shows the distribution of CD8+T cell subsets, the response to NACI treatment, and the clone size across lineages. MPR, major pathological response; NMPR, non-MPR; scCODA, a Bayesian model for compositional single-cell data analysis; Tpex, progenitor exhausted T cells; Trm, tissue-resident memory T cells; UMAP, uniform manifold approximation and projection.

## Oligoclonal persistence enables cytotoxic revival in NACI-responsive T cells

Longitudinal TCR tracking revealed divergent clonal dynamics underpinning therapeutic outcomes. In the MPR group, pretreatment-persisting CD8+T cell clones dominated the on-treatment repertoire, exhibiting heightened tumor reactivity signatures that aligned with their oligoclonal expansion patterns (online supplemental figure S4A, figure 3A).<sup>34,35</sup>

Given that persisting T cells are associated with the MPR to NACI treatment, we then reclustered the persisting T cells to investigate any alterations in their phenotypes on treatment with NACI (figure 3B). Compared with total CD8 T cells, persisting T-cell clones presented more pronounced phenotypic characteristics, leading to the identification of an effector memory T-cell subcluster (cluster 1). In addition, persisting T-cell clones presented a similar distribution of clone size to that observed in total CD8+T cell populations, and hyperexpanded clones were exclusive to the MPR sample (figure 3C). Furthermore, NACI treatment significantly elevated the cytotoxic function of persisting T cells in both the MPR and NMMPR samples, whereas T-cell exhaustion was attenuated only in the MPR sample (figure 3D).

Focusing on the top 50 expanded clones, we revealed fundamental divergences in NACI-induced clonal dynamics (online supplemental table S4). MPR-derived clones exhibited a striking oligoclonal architecture, where two hyperexpanded clones constituted 60% of the persisting repertoire, maintaining stable clonal frequencies across treatments (figure 3E and online supplemental figure S4B). These dominant clones underwent a coordinated phenotypic shift toward effector states, with the acquisition of GZMK+effector-memory signatures during treatment while evading CTLA4+terminal exhaustion (figure 3F). In stark contrast, the NMMPR clones remained trapped in pretreatment distributions, maintaining static phenotypic equilibrium between exhaustion and effector states. The dichotomy culminated in MPR-specific cytotoxic revival, marked by the expansion of GZMK+effectors coupled with the attrition of terminal exhausted populations, whereas the NMMPR clones showed neither clonal expansion nor functional enhancement (figure 3G). These data establish oligoclonal persistence coupled with effector reprogramming as a hallmark of a productive NACI response, where selective pressure favors pre-existing tumor-reactive clones capable of escaping terminal exhaustion.

The interplay between clonotypic persistence and phenotype has emerged as a critical determinant of the NACI response.<sup>14</sup> The pretreatment Trm populations (4: TRM) constituted a greater proportion of the MPR clones than the NMMPR clones did (online supplemental figure S4G, p=0.035), with an almost ubiquitous presence in all the MPR clones (figure 3E and online supplemental figure S4G). Pseudotime reconstruction revealed Trm cells as differentiation intermediates capable of differentiating into terminal exhaustion states

(online supplemental figure S4C). Furthermore, cross-subset analysis of persisting T-cell phenotypes revealed a conserved gene module preferentially expressed in MPR samples. This gene set included the canonical Trm markers CXCR6 and ZNF683, leading us to designate it as the response-associated Trm signature (online supplemental figure S4D,E and table S3). The Trm signature remained elevated in MPR samples across scRNA-seq and spatial transcriptomics (online supplemental figure S4F, 3H,I), reflecting preserved tissue-resident memory programs associated with MPR to NACI. Multiplex immunohistochemistry (mIHC) verified the enrichment of CD103+CD8+ Trm cells in MPR versus NMMPR samples (n=3, figure 3J).

## Antitumor immune response-related T-B interactions are augmented in MPR tumors

In addition to CD8+T cell dynamics, CD4+T cell subsets exhibit distinct remodeling patterns that are correlated with therapeutic outcomes.<sup>24,36</sup> Unsupervised clustering revealed six CD4+T cell populations with limited clonal expansion and minimal clonotype sharing (online supplemental figure S5A–C and E). Strikingly, NACI treatment selectively reduced regulatory T cell (Treg) frequencies in MPR samples while upregulating antitumor pathways like interferon (IFN)-γ response (online supplemental figure S5F).

Given the critical role of T-B-cell collaboration in antitumor immunity, we identified six B-lineage subsets (online supplemental figure S6A). NACI increased total B-cell infiltration without dominant subset expansion (online supplemental figure S6B). Among these subsets, naïve B cells (Bn\_FCER2) express an antibody receptor, FCER2 (encoding CD23), associated with mature tertiary lymphoid structures (TLS) and better prognosis.<sup>8</sup> Additionally, germinal center B cells (GCB\_NR4A2) expressed genes crucial for germinal center selection (NR4A1 and NR4A2).<sup>37</sup> Their increase suggests TLS formation post-NACI.

Cell-cell interaction analysis by CellChat<sup>38</sup> revealed enhanced costimulatory signaling such as CD28-CD86 and LIGHT signaling, as well as cytotoxic cytokine circuits in MPR tumors (online supplemental figure S6D). TLS-associated Bn\_FCER2 and GCB\_NR4A2 subsets preferentially engaged exhausted CD8+T cells via CD86 (online supplemental figure S5G, S6F), critical for T-cell activation.<sup>39</sup> In addition, a unique MPR-specific T-B interaction involved IFN-γ-stimulated B cells (B\_ISG\_ISG15) enhancing CD8+T cell function via interleukin (IL)-2 (online supplemental figure S6E). Spatially, MPR samples showed denser T-B cell aggregation and mature TLSs at tumor-stroma interfaces and distal stroma (figure 4H,I), whereas few TLSs were found in NMMPR samples (figures 3J and 4I), indicating spatial proximity enables T-B crosstalk for coordinated antitumor responses.

## Heterogeneity of malignant tumor cells

Residual malignancies frequently harbor DTP cell populations that drive therapeutic resistance through

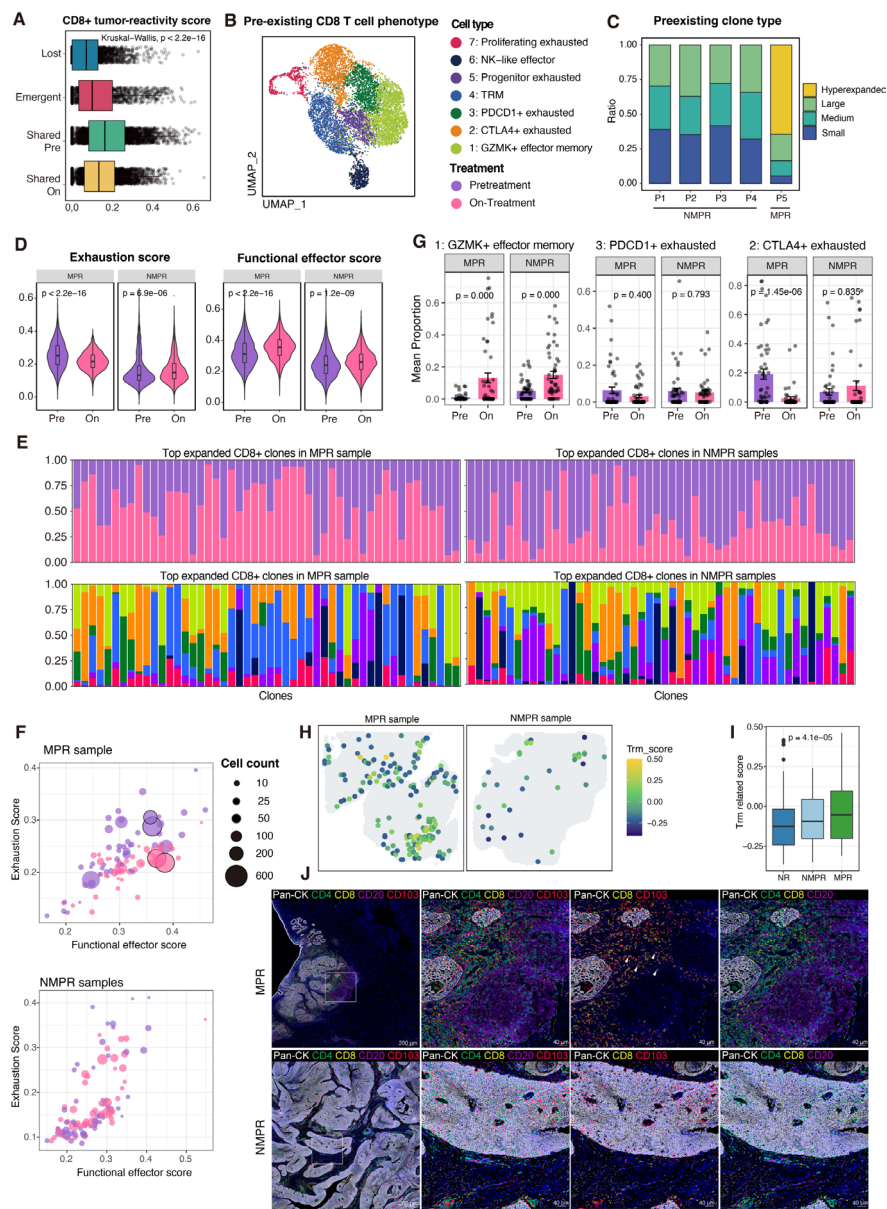


**Figure 3** Phenotypic and clonal alterations of persisting CD8+T cell clones. (A) Boxplots showing the tumor-specific scores of CD8+T cell clones that were lost, emergent, and shared during NACI treatment. Statistical significance was analyzed via the Kruskal-Wallis test. The boxplots display the median, upper quartile, and lower quartile. (B) UMAP plot of persisting CD8 T cells shown as a fraction for each patient. The cell cluster colors are shown in B. (C) Bar plot showing the cellular composition of persisting CD8 T cells shown as a fraction for each patient. The error indicates the SE of measurement ( $n=50$ ). (D) Violin plot showing the alterations in the exhaustion score and functional effector score of CD8+T cell clones in MPR and NMPR tumors during NACI treatment. Statistical significance was analyzed via the Wilcoxon test. (E) Bar plots of the proportions of cells in the indicated phenotype cluster and resources from pretreatment or on-treatment samples among the top 50 expanded clones. (F) Bubble plot showing the alterations in clone size in MPR and NMPR tumors during NACI treatment. The clone size was represented by the size of the bubbles, with the x-axis and y-axis indicating the median functional effector score and exhaustion score, respectively. (G) Bar plot showing the mean proportions of three representative subsets among the highly expanded clones during NACI treatment. The error indicates the SE of measurement ( $n=50$ ). A Wilcoxon test was used to analyze the statistical significance. (H) Distribution of CD8+T cells inferred via CytoSPACE in the ST data. The color reflects the Trm score. (I) Boxplots showing the Trm score among samples with differential responses to NACI. Statistical significance was analyzed via the Kruskal-Wallis test. (J) Representative miHIC images of MPR and NMPR tumor samples, demonstrating the spatial distributions of immune subsets and epithelial cells. The containing panels include CD4 (green), CD8 (yellow), CD20 (purple), CD103 (red), and Pan-CK (white) cells. Nuclei were counterstained with DAPI (blue). The arrows highlight CD8+CD103+ T cells, which are indicative of tumor-reactive tissue-resident memory populations. Scale bars are indicated in the lower-right corner of each panel. CTLA4, cytotoxic T-lymphocyte-associated protein 4; DAPI, 4',6-Diamidino-2-phenylindole; GZMK, granzyme K; miHIC, multiplex immunohistochemistry; MPR, major pathological response; NACI, neoadjuvant chemoimmunotherapy; NK, natural killer; NMPR, non-MPR; NR, non-response; Pan-CK, pan-cytokeratin; PDCD1, programmed cell death protein 1; ST, spatial transcriptomics; Trm, tissue-resident memory T cells; UMAP, uniform manifold approximation and projection.

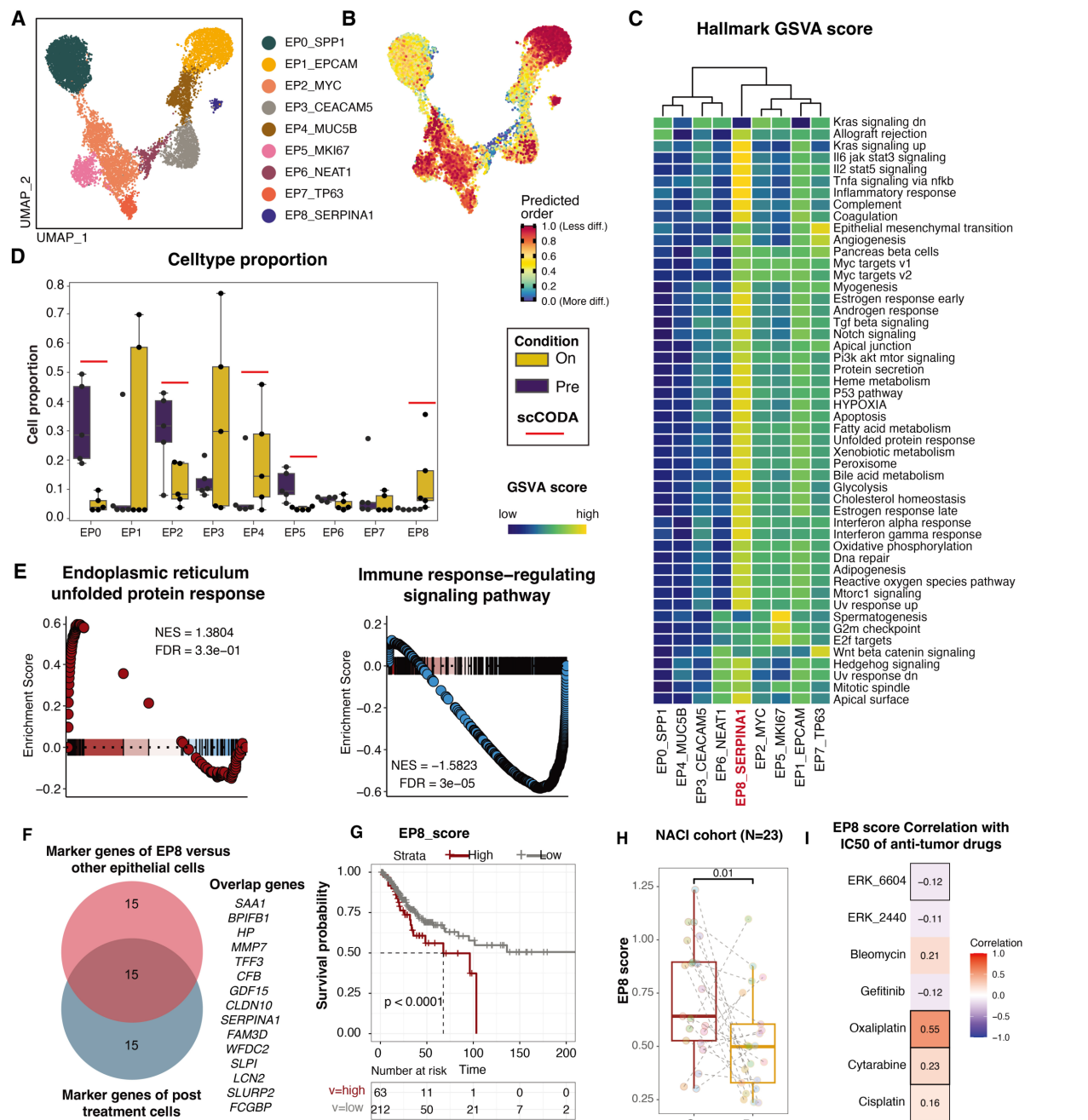


**Figure 4** Epithelial cell reprogramming following NACI. (A) UMAP plot of the epithelial cell subsets (denoted by colors). (B) UMAP plot of the extent of epithelial cell differentiation. The extent of differentiation was predicted by the cytoTRACE. Dark green indicates a relatively high degree of differentiation, whereas dark red indicates a relatively low degree of differentiation. (C) Heatmap showing the GSVA scores of 50 hallmark gene sets among epithelial subsets. (D) Boxplots showing the changes in the proportions of each epithelial subset before and after treatment. Statistical significance was analyzed via scCoda, with red bars indicating credible and significant results. The boxplots display the median, upper quartile, and lower quartile. (E) GSEA of epithelial cells in on-treatment samples. (F) Comparison and overlap of the top marker genes of the EP8 subset and epithelial cells in the on-treatment samples. The numbers indicate the number of genes in each set. The genes that are shared between both sets are indicated. (G) Kaplan-Meier survival analysis of the EP8 signature in the TCGA CESC cohort (n=304). The survival curves were compared via the log-rank test. (H) Boxplots showing the EP8 scores of pretreatment and on-treatment samples from the NACI study (n=23). The colors indicate the patients, and the paired samples are connected by dashed lines. (I) Correlation analysis between the EP8 signature and IC50 values in cervical cancer cell lines treated with various pharmacological agents. The statistical significance of the observed correlation was determined by a two-sided Pearson correlation test. Bolded borders indicate  $p < 0.05$ . CESC, cervical squamous cell carcinoma and endocervical adenocarcinoma; Diff, differentiated; EP8, epithelial subcluster 8; FDR, false discovery rate; GSEA, gene set enrichment analysis; GSVA, gene set variation analysis; IC50, half-maximal inhibitory concentration; NACI, neoadjuvant chemoimmunotherapy; NES, normalized enrichment score; scCoda, a Bayesian model for compositional single-cell data analysis; TCGA, the cancer genome atlas; UMAP, uniform manifold approximation and projection.

incomplete responses to systemic treatments.<sup>18</sup> To investigate this transient phenotype in CC under NACI, we first mapped epithelial cell heterogeneity across treatment phases. Using established biomarkers<sup>40</sup> for cellular origin and malignant potential (figure 4A, online supplemental table S2), we delineated seven distinct epithelial subsets: classical squamous carcinoma (EP2\_MYC), adenocarcinoma (EP3\_CEACAM5 and EP4\_MUC5B), proliferative (EP5\_MKI67), invasive (EP7\_TP63), and notably, a novel macrophage–tumor fusion population (EP0\_SPP1), which is consistent with the reported immune evasion mechanism of Zhang *et al.*<sup>41 42</sup> Intriguingly, we identified a SERPINAL1-enriched subset encoding α-1-antitrypsin, a multifunctional mediator of tumor progression and immune suppression.<sup>43 44</sup>

Differentiation state analyses further identified EP2, EP5, EP7, and EP8 as poorly differentiated subpopulations (figure 4B). Hallmark pathway analysis through gene set variation analysis (GSVA) validated subtype specificity: EP5 showed enriched proliferation signatures, such as the G2M checkpoint and E2F targets. EP7 activated epithelial–mesenchymal transition, whereas EP2 exhibited broad pathway activation across multiple oncogenic programs (figure 4C). To identify tumor cells from epithelial populations, we performed copy number variation (CNV) inference using endothelial cells as the reference (online supplemental figure S7A). CNV profiling classified all epithelial subpopulations as tumor cells and revealed distinct genomic landscapes. EP2 and EP5 displayed elevated CNV scores, indicating increased genomic instability, whereas the on-treatment samples presented reduced CNV burdens (with the exception of patient 1), suggesting a reduction in overall genetic aberrations following treatment (online supplemental figure S7B,C).

#### A persistent tumor subset exhibited endoplasmic reticulum stress characteristics

The dynamic reorganization of epithelial subpopulations under therapeutic pressure revealed critical persistence mechanisms. The proportions of EP2, EP4, and EP5 significantly decreased in the on-treatment samples, indicating that the treatment was sensitive to these subsets. In contrast, the EP8 subset was predominantly identified in the on-treatment samples (figure 4D). Transcriptomic profiling revealed three hallmarks of EP8 persistence: (1) Pronounced activation of endoplasmic reticulum (ER) stress and the unfolded protein response (UPR) under chemical stress.<sup>45</sup> Transcription factor regulation prediction revealed that *XBP1*, a key transcription factor in the unfolded protein response, was specifically regulated in the on-treated samples (online supplemental figure S7E). (2) Coordinated suppression of immune-regulatory pathways (figure 4E), and (3) emergence of a gene signature shared by each subset in on-treatment samples (online supplemental figure S7D and figure 4F).

A signature for EP8 was thus defined, comprising genes associated with ER stress, including SAA1 and GDF15,<sup>46 47</sup>

and correlated with poor survival in The Cancer Genome Atlas (TCGA) -cervical squamous cell carcinoma and endocervical adenocarcinoma (CESC) cohort (figure 4G). Multimodal validation confirmed the NACI-induced EP8-related gene signature. The bulk RNA-seq data, which included paired tumor samples obtained before and after the administration of NACI (N=23), revealed significant increases in EP8 activity scores in the on-treatment samples (figure 4H), whereas the STs presented greater EP8 signals in the NMPR samples (online supplemental figure S7G,H). Functional interrogation via Genomics of Drug Sensitivity in Cancer, a pharmacogenomic database, revealed that EP8<sup>high</sup> CC cell lines exhibit platinum resistance but heightened vulnerability to extracellular signal-regulated kinase (ERK) and mitogen-activated protein kinase (MAPK) inhibition (figure 5I), suggesting that ER stress-mediated MAPK activation may drive therapeutic escape. Additionally, in another single-cell dataset comprising fifteen treated-naïve CC samples, the classic squamous cell carcinoma feature (EP2) and proliferating feature (EP5) were identified, yet the EP8 score was elevated among all epithelial subsets (online supplemental figure S7F).

#### A pre-existing proinflammatory program impedes the NACI response in MNPR tumors

Stratification of tumor-infiltrating myeloid populations revealed four tumor-associated macrophage (TAM) subtypes (online supplemental figure S8A), alongside distinct mast cells, neutrophils, and three dendritic cell subsets (figure 5A,B).<sup>48</sup> Comparative analysis revealed fundamental compositional divergence between NMPR and MPR tumors, particularly in terms of macrophage and mast cell infiltration dynamics (figure 5C). The distributions of myeloid cell types across response and treatment groups were further verified in the NACI cohort and murine model (figure 5D,E). Both MPR tumors in our cohort and complete response samples in the NACI cohort (figure 5D) exhibited preferential enrichment of the lipid-associated Macro\_CCL18 subtype, which paradoxically coexpressed *CCL18* with enhanced major histocompatibility complex (MHC) class II complex components and CCR5-targeting chemokines (online supplemental figure S8B). While maintaining immunosuppressive properties through *CCL18* secretion, Macro\_CCL18 simultaneously acquires antigen-presenting capacity and T-cell chemoattractant potential via CCR5 ligand production. *CCL18*-mediated adaptive immunity modulation provides mechanistic insight into differential treatment outcomes, positioning Macro\_CCL18 as a potential biomarker of successful antitumor responses. Conversely, the Macro\_IL1B subtype emerged as a treatment-resistant phenotype, persisting in pretreatment NMPR tumors and all on-treatment samples. This proinflammatory population demonstrated characteristic *IL1A* and *IL1B* overexpression alongside the neutrophil-recruiting chemokines *CXCL2* and *CXCL3*.

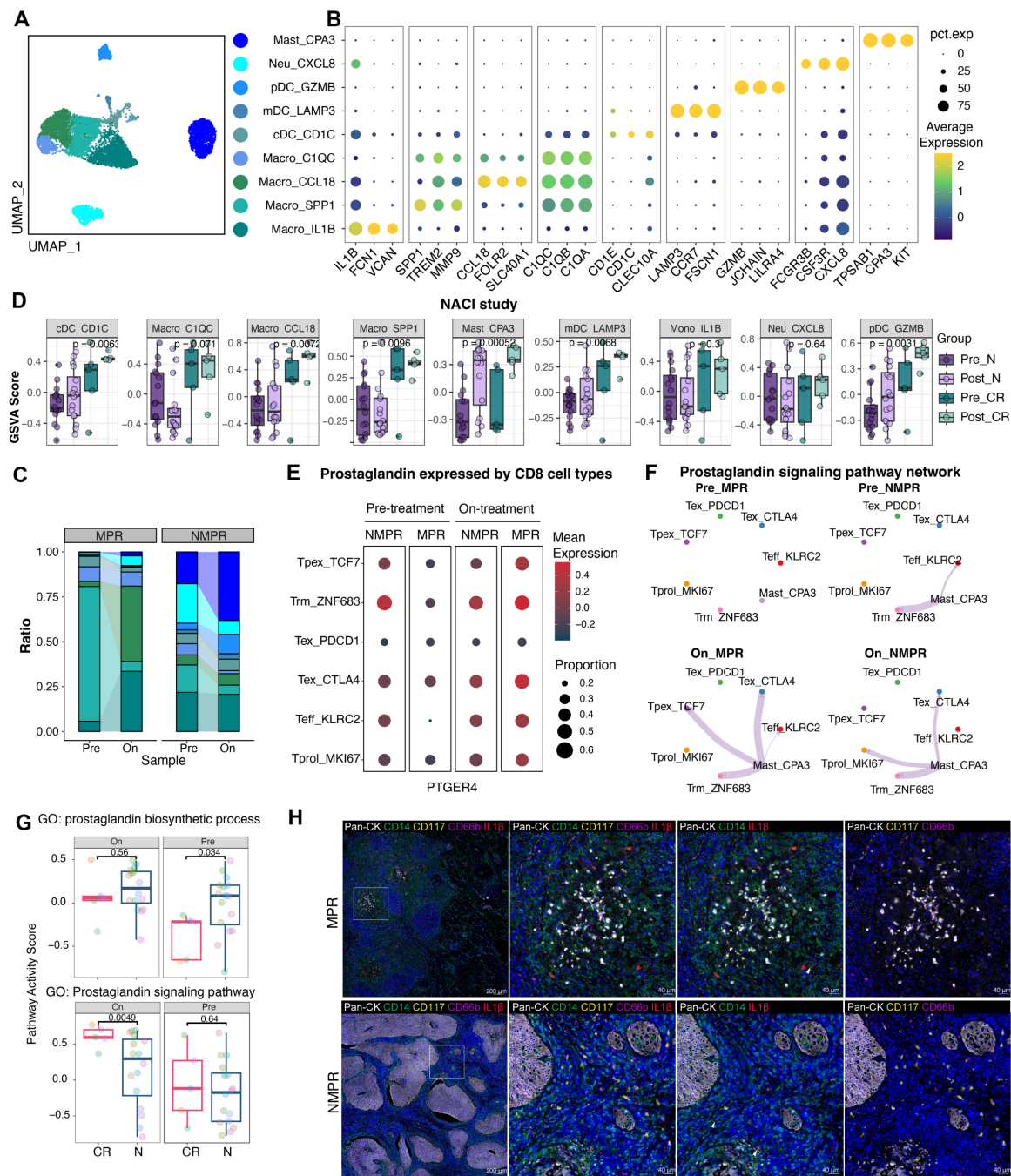


**Figure 5** Proinflammatory myeloid cells enriched in NMPR tumors before treatment. (A) UMAP plot of myeloid subsets (denoted by colors). (B) Dot plots showing marker genes of myeloid subsets. The diameter of the dot represents the proportion of cells expressing the given gene, with colors indicating the level of expression, normalized to a Z score. (C) Alterations in myeloid cellular composition after treatment for MPR and NMPR patients. The cell cluster colors are shown in figure 6A. (D) Boxplots showing the GSVA scores of the myeloid subset signature in the NACI cohort ( $n=23$ ). The boxplots display the median, upper quartile, and lower quartile. Statistical significance was analyzed via the Kruskal-Wallis test. (E) Dot plots showing the normalized PTGER4 expression of CD8+T cells in MPR and NMPR tumors during NACI treatment. The diameter of the dot represents the proportion of cells expressing the given gene, with colors indicating the level of expression. (F) Circle plots showing the prostaglandin signaling inferred by cellChat among mast cells and CD8+T cell subsets in MPR and NMPR tumors during NACI treatment. (G) GSVA score for prostaglandin-related pathways in CR and non-complete response (N) samples from the NACI study. A Wilcoxon test was used to analyze the statistical significance. (H) Representative miHIC images of MPR and NMPR tumor samples, demonstrating spatial distributions of myeloid subsets and epithelial cells. The containing panels include the following: CD14 (green), CD117 (yellow), CD66b (purple), IL1 $\beta$  (red), and Pan-CK (white). Nuclei were counterstained with DAPI (blue). Scale bars are indicated in the lower-right corner of each panel. CR, complete response; DAPI, 4',6-Diamidino-2-phenylindole; GO, gene ontology; GSVA, gene set variation analysis; IL, interleukin; miHIC, multiplex immunohistochemistry; MPR, major pathological response; NACI, neoadjuvant chemoimmunotherapy; NMPR, non-MPR; Pan-CK, pan-cytokeratin; PTGER4, prostaglandin E receptor 4; UMAP, uniform manifold approximation and projection.

(online supplemental figure S8B), mirroring the inflammatory TAM signature established in mismatch repair-deficient colorectal cancers.<sup>12</sup>

The presence of tumor-infiltrating mast cells has been linked to a reduced response to anti-PD-1 therapy in a murine model,<sup>49</sup> although the mechanistic understanding remains limited. Our single-cell profiling revealed mast cell accumulation specifically in NMPR tumors post-NACI treatment, in contrast with their minimal presence in MPR lesions (figure 5C). Intriguingly, bulk RNA-seq analysis of the NACI cohort revealed that chemoimmunotherapy triggered a marked increase in mast cell infiltration.

Functional characterization revealed a prostaglandin metabolic profile in mast cells, concurrent with suppressed T-cell cytotoxicity signatures (online supplemental figure S8F). This observation is clinically relevant given the established role of prostaglandin E2 (PGE<sub>2</sub>) in CD8+T cell suppression via PTGER2/4 signaling.<sup>21</sup> Following NACI treatment, PTGER4 expression was elevated in both the MPR and NMPR T-cell subsets. However, prior to treatment, PTGER4 expression was notably greater in NMPR T cells than in MPR T cells, particularly in the tissue-resistant T-cell subset (figure 5F). Cell-cell interaction analyses confirmed the absence of mast cell-T-cell prostaglandin signaling networks in pretreated MPR tumors (figure 5G), whereas bulk RNA-seq further revealed that prostaglandin biosynthesis activation was associated with an incomplete NACI response (figure 5H).

While myeloid populations typically orchestrate immunosuppressive networks,<sup>50</sup> our interaction analysis revealed therapeutic context-dependent reprogramming.<sup>31</sup> Through ligand-receptor co-expression mapping,<sup>31</sup> we identified CCR1/CC5-driven myeloid-CD8+T cell chemotaxis as a hallmark of MPR tumors (online supplemental figure S8D). This immunostimulatory phenotype contrasts sharply with that of NMPR lesions, where myeloid-epithelial crosstalk via IL1-A/B-NF-κB axis activation predominates,<sup>52</sup> suggesting microenvironment-driven lineage plasticity. The clinical significance of this dichotomy emerged through correlative analyses: CCL18+macrophages (enriched in the MPR) were positively associated with PD-1+CD8+ T cell infiltration, whereas NMPR-prevalent mast cells and neutrophils were inversely correlated with cytotoxic T-cell populations (online supplemental figure S8E).

The mIHC staining of myeloid markers validated our single-cell profiling data, revealing pronounced infiltration of IL-1β+CD14+ macrophages, neutrophils, and mast cells in NMPR tumors. In contrast, MPR lesions presented a significantly reduced presence of these proinflammatory myeloid populations (figure 5I). The coordinated enrichment of these interacting myeloid subsets in NMPR-treated tumors suggests a synergistic mechanism of NACI resistance, potentially mediated through their shared capacity for prostaglandin secretion and T-cell suppression.

## Residual tumor cells orchestrated an immunosuppressive niche by interacting with myeloid cells

Spatially resolved transcriptomic profiling of residual lesions revealed dynamic spatial remodeling between malignant cells and myeloid compartments (figure 6A). The proximity index was used to quantify the proximity of a given epithelial spot to each myeloid subset.<sup>53</sup> In NR/NMPR specimens, malignant cells maintained intimate spatial coupling with Macro\_IL1B+macrophages, whereas MPR lesions exhibited predominant malignant-Macro\_CCL18 colocalization, and these findings are concordant with our single-cell data (figure 6B). Furthermore, immunosuppressive subsets, including neutrophils and LAMP3<sup>+</sup> dendritic cells,<sup>54</sup> exhibited a greater proximity index in samples designated as NMPR or NR than in the MPR sample. Moreover, EP8-high epithelial spots (online supplemental figure S9A) showed pronounced spatial colocalization with immunosuppressive myeloid subsets such as Macro\_IL1B, neutrophils, mast cells, and mDC\_LAMP3, a finding quantified by distance analysis confirming their significant proximity (figure 6C). These findings indicate that DTP cells might exploit myeloid cells to establish an immunosuppressive niche.

Cell-cell interaction analyses revealed therapy-induced epithelial-myeloid signaling adaptations, including neutrophil recruitment via CXCR2 axis activation and the presence of two resistance-related pathways, GDF15-TGFBR2 and SAA1-FPR2 signaling (online supplemental figure S9B). These mechanisms showed striking spatial-temporal specificity, emerging exclusively in on-treatment NMPR samples and correlating with EP8+malignant cell signatures. The GDF15-TGFBR2 interaction exhibited particular clinical relevance, as increased ligand-receptor co-expression was detected in NMPR lesions compared with MPR lesions (online supplemental figure S9C). This aligns with established paradigms of TGF-β-mediated myeloid reprogramming<sup>55</sup> and the role of GDF15 in establishing immune-excluded niches.<sup>56</sup>

The colocalization of GDF15<sup>+</sup> epithelial cells and TGFBR2<sup>+</sup> myeloid cells was more prevalent in the NR or NMPR samples than in the MPR samples (figure 6D-F), while SAA1-FPR2 signaling was also enriched in the NR and NMPR samples (figure 6G). Cell-cell communication networks at the spatial level were also constructed to verify our findings (online supplemental figure S10A). The NMPR sample presented the greatest number of cellular interactions, indicative of a hyperconnected network related to resistance. GDF15-TGFBR2 signaling was also detected in the NR and NMPR samples (online supplemental figure S10B,C), whereas the MPR sample showed no significant interactions in this signaling pathway. This spatial colocalization suggests that DTP cells orchestrate myeloid reprogramming via activation of the GDF15-TGFBR2 axis, thereby promoting immune-evasive myeloid-DTP niches.

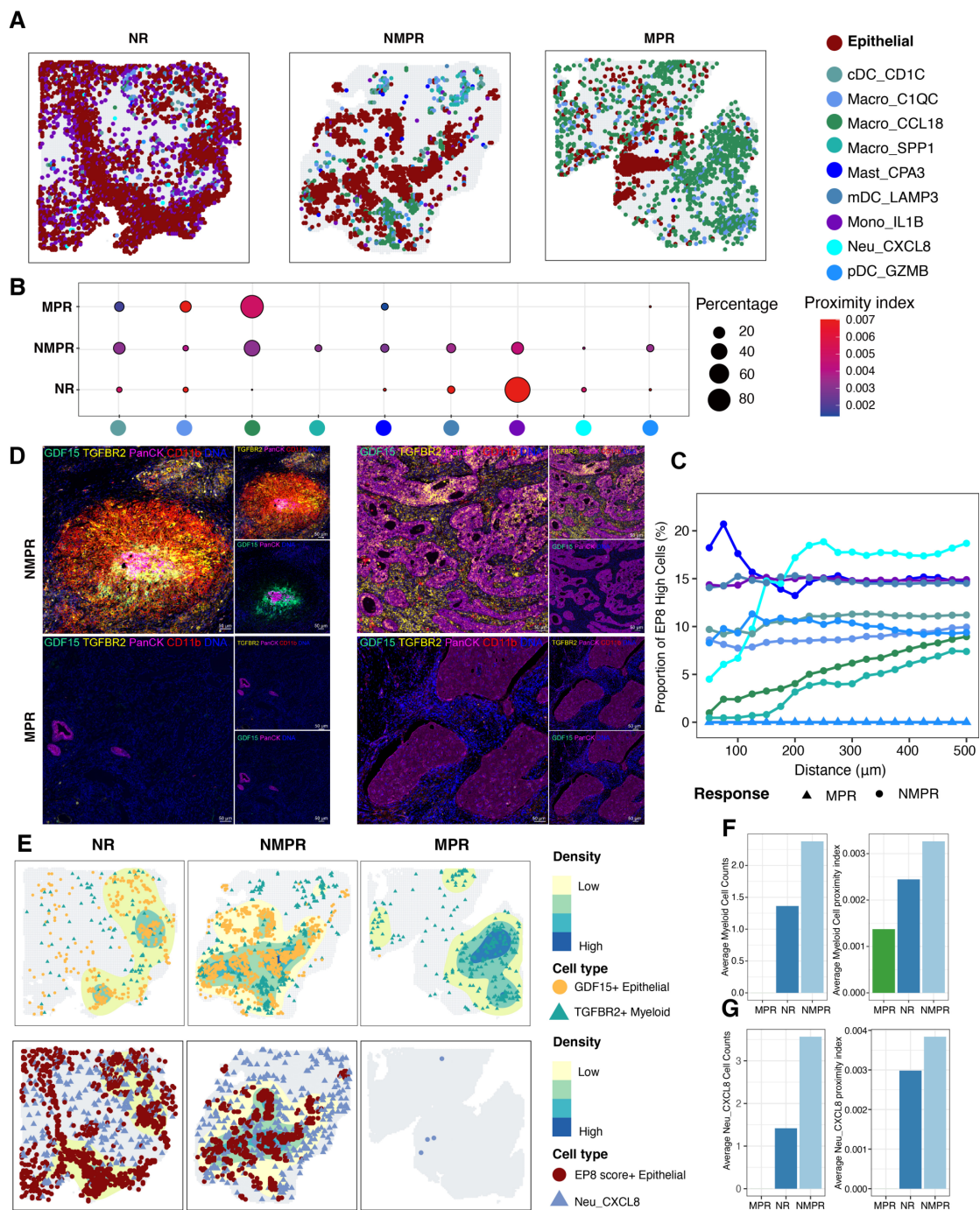


**Figure 6** Residual tumor cells exhibited spatial proximity to immunosuppressive myeloid cells. (A) The cell distribution of the myeloid subsets and epithelial cells in the ST data. The presence of epithelial cells was inferred via a cytovisual. Myeloid subsets were identified by using the highest-scoring myeloid subset signature from the scRNA-seq data. (B) Dot plot showing the spatial proximity between epithelial cells and myeloid cells in the ST data. The size of the circle represents the percentage of epithelial cells that are in closest proximity to each myeloid subset, and the color indicates the median proximity index between epithelial cells and each myeloid subset. (C) Spatial proximity between the high EP8 epithelial spots and the myeloid subsets. The x-axis represents the varying radius centered on the myeloid cells. The y-axis of the figure indicates the probability of high EP8 epithelial cells manifesting in proximity to myeloid subsets. (D) Representative mIHC images of MPR and NMPR tumor samples, demonstrating spatial distributions of myeloid subsets and GDF15+epithelial cells. The containing panels include the following: GDF15 (green), TGFBR2 (yellow), Pan-CK (purple) and CD11b (red). Nuclei were stained with DAPI (blue). Scale bars are indicated in the lower-right corner of each panel. (E) Spatial colocalization of GDF15+epithelial cells with TGFBR2+myeloid cells (upper) and EP8+epithelial cells with neutrophils (lower) in ST samples. The color gradient indicates the density of colocalized cells. (F–G) Bar plot depicting the average myeloid cell counts and proximity indices of epithelial cells in the ST samples. DAPI, 4',6-Diamidino-2-phenylindole; EP8, epithelial subcluster 8; GDF15, growth differentiation factor 15; mIHC, multiplex immunohistochemistry; MPR, major pathological response; NMPR, non-MPR; NR, non-response; scRNA-seq, single-cell RNA sequencing; Pan-CK, pan-cytokeratin; ST, spatial transcriptomics; TGFBR2, transforming growth factor beta receptor 2.

## Experimental validation on IRE1 $\alpha$ /XBPI-mediated DTP phenotype

We further established chemotherapy treatment models using CC cell lines (SiHa and ME180) under low-dose cisplatin or oxaliplatin exposure. Both platinum agents increased spliced XBPI and ERN1 (encoding IRE1 $\alpha$ ) mRNA levels across the cell lines (figure 7A). Concomitantly, the EP8-associated secretory proteins SERPINA1, SAA1, and GDF15 exhibited dose-dependent upregulation at both the mRNA and protein levels (figure 7A,B). Notably, combination with 4 $\mu$ 8C, a selected IRE1 inhibitor, synergistically enhanced chemosensitivity, reducing the half-maximal inhibitory concentration (IC50) values of cisplatin and oxaliplatin in the ME180 cell line (figure 7C). In TC-1 syngeneic model mice (n=5), 4 $\mu$ 8C combined with chemotherapy and an anti-PD-1 antibody significantly suppressed tumor progression compared with chemotherapy alone, whereas the addition of an anti-PD-1 antibody had limited efficacy (figure 7D–G). Moreover, cotreatment with 4 $\mu$ 8C markedly attenuated EP8-associated secretory phenotypes, such as SAA1, GDF15 and SERPINA1 (figure 7H).

To delineate the impact of chemoimmunotherapy on TME remodeling and evaluate the therapeutic potential of the IRE1 $\alpha$ /XBPI inhibitor 4 $\mu$ 8C, we performed RNA sequencing on tumor specimens from a murine model subjected to distinct treatment regimens (n=3). GSVA revealed that chemotherapy significantly increased CD8+T cell infiltration, while combination with anti-PD-1 immunotherapy further augmented the transcriptional activity of progenitor-exhausted CD8+T cell populations (figure 7I). Chemoimmunotherapy also triggered a marked increase in mast cell infiltration and cotreatment with the IRE1 $\alpha$ /XBPI inhibitor 4 $\mu$ 8C attenuated this effect (figure 7J). These findings suggest that XBPI signaling may orchestrate mast cell recruitment during therapy and that its suppression could counteract immune-evasive microenvironment remodeling.

Notably, chemotherapy upregulated EP8-associated transcriptional signatures, whereas coadministration of 4 $\mu$ 8C abrogated these effects, suppressing both the EP8 signature and IRE1 $\alpha$ /XBPI pathway activation (figure 7K). To further determine whether the EP8 signature is transcriptionally regulated by XBPI, we analyzed XBPI chromatin immunoprecipitation sequencing (ChIP-seq) datasets derived from the hepatocellular carcinoma HepG2 cell line. This revealed that XBPI binds directly to the promoter region of GDF15, with no significant occupancy observed at other EP8-associated loci (figure 7L). These results identify GDF15 as the sole direct transcriptional target of XBPI within the EP8 network, implicating GDF15 as a critical mediator of DTP cell-driven immune evasion, which is consistent with previous evidence that neutralization of GDF15 synergizes with anti-PD-1 therapy.<sup>57</sup> These findings demonstrate that XBPI/IRE1 $\alpha$ -mediated ER stress coordinates both chemoresistance and immune evasion in EP8-enriched

tumors, suggesting that targeting IRE1 $\alpha$ /XBPI pathway or GDF15 may overcome NACI resistance in CC.

## DISCUSSION

Single-cell dissection of the TME has been considered a critical tool for deciphering cancer immunotherapy mechanisms. Our study provides the first comprehensive atlas of cellular dynamics and spatial reorganization in locally advanced CC during NACI, integrating paired pretreatment/on-treatment scRNA-seq and scTCR-seq data to reveal the adaptive immune signatures in MPR tumors and immune evasion mechanisms of residual tumor cells.

While the synergistic effects of chemotherapy and immunotherapy have been extensively studied through immunogenic cell death (ICD) mechanisms,<sup>58 59</sup> most evidence has been derived from preclinical models or histopathological analyses. Recent single-cell studies in clinical trial cohorts<sup>17</sup> have revealed the dual role of chemotherapy in reshaping TME immunogenicity. Notably, the interplay between chemotherapy and immunotherapy presents cancer type-specific paradoxes: monotherapy with paclitaxel was shown to reduce the abundance of key immune subsets that are responsive to paclitaxel in combination with atezolizumab,<sup>60</sup> whereas the clonal expansion of GZMK+Tpex cells with chemoimmunotherapy has been demonstrated in non-small cell lung cancer.<sup>10</sup> Compared with pre-existing T cells, our CC cohort receiving the platinum–paclitaxel–anti-PD-1 combination presented limited Tpex expansion characterized by reduced tumor specificity and exhaustion. These data suggested that pre-existing clones dominated NACI responsiveness. Consequently, the administration of platinum plus paclitaxel had minimal synergistic effects on immunosurveillance in tumors without the presence of expanded T-cell clones, underscoring the prognostic value of the baseline TME composition.

Additionally, we observed an increase in the cellular stress response following NACI treatment. The cellular stress response state, as indicated by the expression of the heat shock genes HSPA1A and HSPA1B, has recently been linked to immunotherapy resistance.<sup>33</sup> This status was observed not only in CD4+ and CD8+ T cells but also in B cells, suggesting a generalized stress response of lymphocytes in response to drug regimens or alterations in the TME, such as hypoxia.<sup>61 62</sup> Therefore, although preliminary clinical trials have demonstrated that the combination of chemotherapy can increase the efficacy of ICIs in patients with CC, it is crucial to elucidate the independent effects of chemotherapy and ICI regimens to facilitate more informed clinical decisions and reduce the treatment burden.

ER stress adaptation mediated by residual tumor cells warrants particular attention. Chemotherapeutics such as cisplatin or paclitaxel induce ER stress-mediated cell death<sup>63</sup> but survive in CC cells via the UPR and increase drug efflux.<sup>64</sup> Our findings indicate that a subset of residual

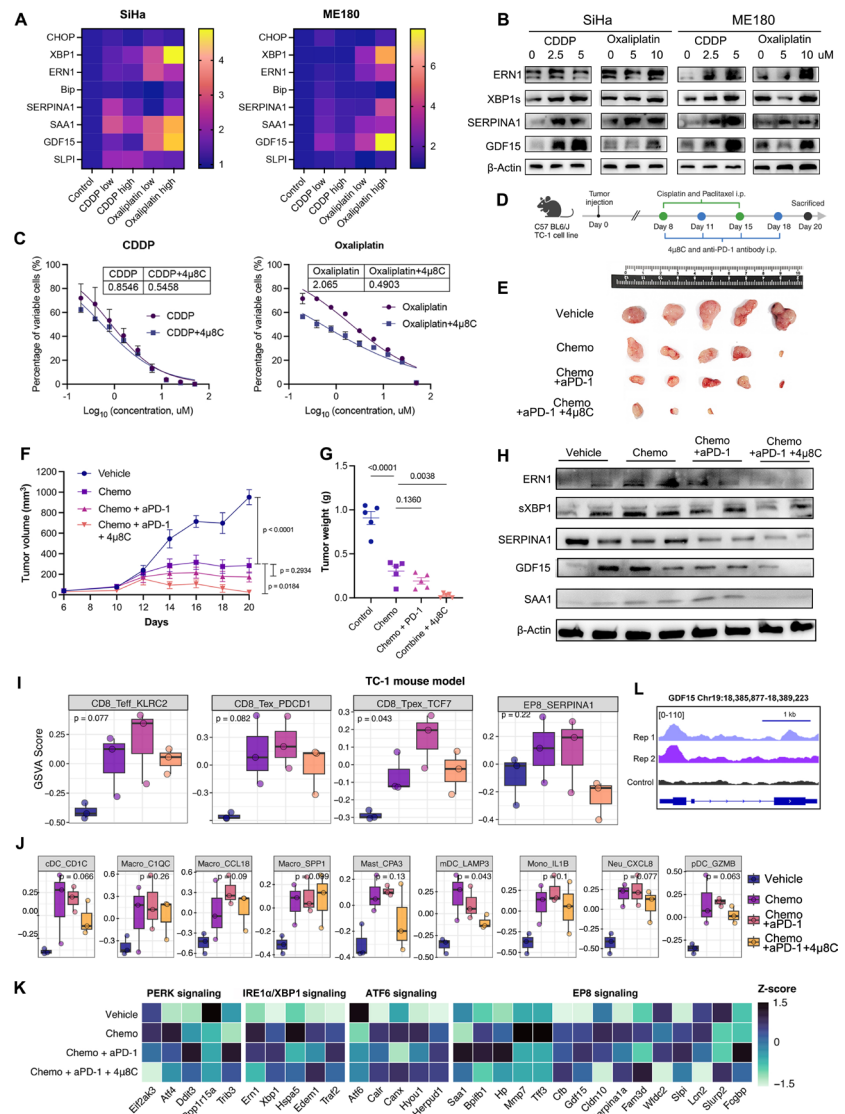


**Figure 7** ER stress activation drives chemoresistance and immune evasion in cervical cancer. SiHa and ME180 cells were treated with low-dose cisplatin (1  $\mu$ M), high-dose cisplatin (2  $\mu$ M), low-dose oxaliplatin (2.5  $\mu$ M) or high-dose oxaliplatin (5  $\mu$ M) for 24 hours in 6-well plates, and alterations in ER stress-related genes or EP8 signature genes at the mRNA (A) or protein (B) level were further detected. (A) Heatmap visualization of miRNA levels in SiHa and ME180 cervical cancer cells treated with chemotherapy for 24 hours. The values represent log<sub>2</sub>-transformed fold changes relative to untreated controls. The data were normalized to those of ACTB (mean $\pm$ SEM, n=3). (B) Western blot showing dose-dependent upregulation of ER stress and EP8-associated secretory proteins in cells treated as described in (A).  $\beta$ -actin served as a loading control. (C) CCK-8 viability assays after 24 hours of drug exposure demonstrating synergistic chemosensitivity in ME180 cells treated with cisplatin or oxaliplatin combined with the IRE1 $\alpha$  inhibitor 4 $\mu$ 8C (10  $\mu$ M). (D) Schematic of the in vivo experimental design. (E) Endpoint tumor volumes in TC-1 syngeneic mice (n=5) treated with vehicle, chemotherapy only (cisplatin 1.5 mg/kg+paclitaxel 15 mg/kg, weekly), combination therapy (chemotherapy+anti-PD-1 200  $\mu$ g biweekly), or triple therapy (combination therapy+4 $\mu$ 8C 10 mg/kg biweekly). All regimens were injected intraperitoneally. (F) Tumor growth curves (mean $\pm$ SEM) of the tumors in the mice described in (E). Endpoint tumor volumes were analyzed by two-way ANOVA with Tukey's post hoc test (n=5). P values are indicated in the figure. (G) Endpoint tumor weights (means $\pm$ SEMs) of the tumors in the mice described in (E). Statistical significance was analyzed by two-way ANOVA with Tukey's post hoc test (n=5). P values are indicated in the figure. (H) Western blot showing dose-dependent upregulation of ER stress and EP8-associated secretory proteins in the tumors of the mice treated as described in (D).  $\beta$ -actin served as a loading control. (I–J) Boxplots showing the GSVA scores of the CD8, EP8 subset signatures (I) and myeloid subsets (J) in the TC-1 syngeneic mice (n=3). The boxplots display the median, upper quartile, and lower quartile. Statistical significance was analyzed via the Kruskal-Wallis test. (L) Heatmap displaying the expression profiles of ER stress signaling and EP8 signature genes. The samples are grouped in figure 6E (n=3). Gene expression values were Z score normalized. (K) IGV snapshot illustrating the chromatin occupancy of XBP1 at the GDF15 locus. ANOVA, analysis of variance; ATF6, activating transcription factor 6; CDDP, cisplatin; EP8, epithelial subcluster 8; ER, endoplasmic reticulum; GSVA, gene set variation analysis; IGV, Integrative Genomics Viewer; i.p., intraperitoneal; IRE1 $\alpha$ , inositol-requiring enzyme 1 alpha; ME180, human cervical cancer cell line; PD-1, programmed cell death protein 1; PERK, protein kinase R-like ER kinase; SiHa, human cervical cancer cell line; TC-1, mouse lung epithelial cell line transfected with HPV-16 E6/E7 oncogenes; .

tumor cells (EP8) secretes SAA1 and GDF15 to recruit immunosuppressive myeloid cells. While ER stress or UPR activation is recognized as a tumor survival strategy,<sup>45 65 66</sup> the immunosuppressive or antitumor effects of ER stress are contingent on its intensity.<sup>67</sup> The persistence of mild ER stress in cancer cells has been linked to the triggering of a proinflammatory phenotype, which is mediated by the activation of NF-κB signaling.<sup>67</sup> This involves IL-1β, IL-6, IL-23, and PGE<sub>2</sub>, which have been proven to impair antitumor immunity.<sup>68</sup> However, markedly elevated ER stress can drive ICD,<sup>69</sup> which ultimately orchestrates an antitumor immune response. The addition of type II ICD inducers to current platinum-based therapeutic regimens may be advantageous, given that neither oxaliplatin nor cisplatin induces significant ER stress. Type II ICD inducers are located primarily in the ER, where they cause oxidative stress or selectively activate the protein kinase R-like ER kinase signaling pathway, which is essential for ICD.<sup>23</sup> Our results further suggest the potential mechanisms by which residual tumor cells evade immuno-surveillance during NACI treatment.

It is now widely acknowledged that myeloid cells play a pivotal role in determining treatment responses.<sup>70</sup> In this study, our data indicated that NMPR-treated tumors presented proinflammatory signatures marked by mast cell infiltration and Macro\_IL1B macrophages, with mast cells demonstrating enhanced prostaglandin signaling that may suppress stem-like CD8+ T cell expansion via IL-2 inhibition.<sup>21 71</sup> A recent study indicated that<sup>IL-1β+</sup> TAM phenotypes can be elicited by the local synergy of PGE<sub>2</sub>.<sup>72</sup> These findings provide further evidence supporting the association between mast cells and the Macro\_IL1B subset in a proinflammatory TME. Furthermore, transmissible ER stress from tumors to myeloid cells can induce the proinflammatory phenotype of myeloid cells.<sup>69</sup> This may provide a potential explanation for the observed increase in mast cells and Macro\_IL1B in both MPR and NMPR tumors, although mechanistic validation requires further investigation.

PD-L1 combined positive score (CPS) remains among the most robust and widely used biomarkers for predicting immunotherapy benefit.<sup>73 74</sup> In the present cohort, CPS was evaluated from post-treatment samples, and it is conceivable that PD-L1 expression was modified by the preceding neoadjuvant chemo-immunotherapy. In our study, the proportion of patients with CPS<1 was 15%, which is comparable to the results of the KEYNOTE-826 trial. However, the COMPASSION-16 trial suggests that patients with CPS<1 may still experience potential clinical benefit,<sup>75</sup> thereby underscoring the intricate nature of PD-L1-based patient selection. These observations underscore the necessity for a nuanced approach when determining PD-L1 status for treatment decision-making. Another significant avenue involves the identification of more stable and predictive biomarkers from pretreatment specimens, with the potential to integrate CPS with advanced immune signatures to enhance patient stratification and optimize therapeutic benefit.

Our study has several limitations that warrant consideration. First, the sample size of this study is indeed small. Cohort size constraints require validation in larger trials. Second, owing to the limited tumor volume, samples were only able to be collected after the initial course of treatment to ensure sample matching. Longitudinal sampling gaps necessitate serial biopsies to map TME dynamics. Ultimately, combination therapy complexity mandates head-to-head comparisons of individual regimens to resolve synergistic or antagonistic effects.

In conclusion, by mapping single-cell and spatial TME remodeling during NACI, this study advances our understanding of response heterogeneity in CC while providing a framework for regimen optimization. Targeting the IRE1α/XBP1-GDF15 axis to disrupt immunosuppressive niches is a potential strategy for overcoming DTP resistance and improving MPR rates. This mechanistic insight identifies anti-GDF15 antibodies and IRE1α/XBP1 inhibitors as high-priority candidates for combinatorial therapeutic development.

## MATERIALS AND METHODS

### Patient cohort and biospecimen collection

From December 2022 through July 2023, treatment-naïve patients diagnosed with advanced or locally advanced CC were enrolled in this study at Shanghai East Hospital. Prior to undergoing evaluation for surgical intervention, patients received one to four cycles of neoadjuvant immunotherapy (platinum-based chemotherapy plus PD-1 antibody per 3 weeks). Following completion of neoadjuvant chemo-immunotherapy, all patients except Patient 2 underwent open laparotomy, entailing radical hysterectomy plus pelvic lymphadenectomy, along with para-aortic lymphadenectomy. Patient 2, who was deemed unsuitable for surgical intervention based on clinical reassessment, received concurrent chemoradiotherapy.

All participants in the study provided written informed consent. The clinical trial on participants has been registered at the Chinese Clinical Trial Registry (registration number: ChiCTR2300072535). Single-cell sequencing and spatial transcriptomics were used to delineate the characteristics of the TME in these patients. In the scRNA-seq cohort, tumor biospecimens were prospectively collected before and after the first cycle of neoadjuvant immunotherapy under colposcopy (n=10). Samples in the ST cohort were obtained through surgical resection after completion of the last cycle of drug administration (n=3).

### Single-cell RNA sequencing preparation

Fresh tumor tissues from the cervical lesions were obtained via biopsy forceps. To generate a single-cell suspension, the tissue was processed according to a previously established protocol.<sup>40</sup> The tissue was washed twice with precooled Dulbecco's Modified Eagle Medium (DMEM, Gibco, Cat. No. A1451801) supplemented with 0.04% bovine serum albumin (Miltenyi Biotec, Cat. No.

1000076). Next, the tissue was minced into approximately 0.5 mm<sup>3</sup> pieces via ophthalmic scissors. These tissue fragments were then dissociated in a cocktail containing collagenase type IV (Gibco, Cat. No. 17104019) and collagenase type I (Gibco, Cat. No. 17018029) for 30 min at 37°C. The resulting cell suspension was filtered through a 40 µm cell strainer (Corning, Cat. No. CLS431750) twice. The suspension was subsequently centrifuged at 300×g for 5 min at 4°C to obtain a cellular pellet. To eliminate red blood cells, the pellet was treated with red blood cell lysis solution (MACS, Cat. No. 130–094–183). After standing at 4°C for 10 min, the suspension was centrifuged at 300×g for 5 min. This process was repeated once more to ensure the complete removal of red blood cells. Finally, the pellet was washed with medium and centrifuged at 300×g for 5 min. The resulting cells were resuspended in 100 µl of medium, and their concentration and viability were determined via a cell counter (Logos Biosystems, LUNA-II).

### Single-cell RNA sequencing

The concentration of the single-cell suspension was adjusted to 700–1,200 cells/µl, and the single-cell gel beads (GEM) in the emulsion were prepared with Chromium Next GEM Single Cell 5' Reagent Kits V.2.0 (10x Genomics, Cat. No. 1000165) following the manufacturer's instructions. To construct the V(D)J library, 5' TCR transcripts were enriched for TCR profiling via the Single Cell V(D)J Enrichment Kit and Human T-Cell (10x Genomics, 1000005) and then amplified via the Chromium Single-cell Human TCR Amplification Kit (10x Genomics, 1000252). The single-cell RNA and TCR V(D)J libraries were subsequently sequenced via an Illumina Nova-seq 6000 with 150 bp paired-end (PE150) reads.

### scRNA-seq data processing

We employed the Cell Ranger single-cell toolkit (V.7.0.1) to align reads from FASTQ files to the GRCh38 human reference genome, resulting in the generation of an initial unique molecular identifier (UMI) matrix. This matrix was subsequently processed via Seurat (V.4.2.1) for quality control. To eliminate low-quality cells, we applied specific filtering criteria: cells were retained only if they had (1) more than 1000 UMIs, (2) fewer than 500 expressed genes, and (3) fewer than 25% UMIs derived from mitochondrial genes. DoubletFinder (V.2.0.3) was used for doublet detection and removal, with an expected doublet rate of 0.08. The predicted doublets were excluded from the gene–barcode matrices. The *normalizeData* function within Seurat was then applied for library-size correction and logarithmic transformation of the expression matrix, which was subsequently used for further downstream analyses.

### Dimension reduction and unsupervised clustering

We conducted dimension reduction and unsupervised clustering via the standard workflow in Seurat, employing default parameters. We performed two-round

unsupervised clustering to identify major cell types and subclusters and to remove the remaining doublets predominantly contaminated with plasma cells. Initially, highly variable genes (HVGs) were identified via the *FindVariableFeatures* function, from which the top 2,000 HVGs were selected for scaling via the *ScaleData* function. Principal component analysis was then performed on the scaled HVG expression matrix via the *RunPCA* function, and the top 20 components were retained for subsequent analyses. The first 15 principal components (PCs) were used in the *FindNeighbors* function. For clustering, the resolution parameter in the *FindClusters* function was set to 0.1 at the first-round clustering. To visualize the data in two dimensions, we applied uniform manifold approximation and projection (UMAP) via the *RunUMAP* function with the same PCs and default parameters. Visualization of the data is achieved via Seurat or Scanpy (V.1.7.2). To observe batch effects among patients in the UMAP plot, we applied the *RunHarmony* function from Harmony to correct for these batch effects.

In the initial clustering round, we employed the *FindAllMarkers* function to identify marker genes for each cluster, using the parameters “min.pct = 0.3” and “thresh.use = 0.3”. Contaminated doublets were detected and removed. We subsequently repeated the dimensional reduction and unsupervised clustering processes. Major cell lineages were assigned to each cell by examining the abundance of canonical marker genes such as *MS4A1*, *CD79B*, *IGHG1*, *CD3E*, *CD3D*, *NKG7*, *ACKR1*, *FLT1*, *PECAMI*, *CDKN2A*, *KRT6A*, *KRT17*, *DCN*, *COL3A1*, *ACTA2*, *CD14*, *FCGR3A*, and *C1QC*. In the second clustering round, we identified specific cell subtypes within each major cell lineage via the aforementioned procedure. The resolution parameter in the *FindClusters* function was adjusted according to the number and nature of the major cell types. To ensure the purity of all the cellular compartments, cell type identification and doublet removal were performed iteratively. The cells retained after the two rounds of clustering were collected for further analysis.

### Proportion analysis

In each sample, the proportion of major cell types was determined by dividing the number of cells within a specific cluster by the total number of cells in the sample. Similarly, the proportions of subclusters within epithelial cells and CD8<sup>+</sup> cells were calculated by dividing the number of cells in each subcluster by the total number of cells in their respective major cell types. To assess differences in relative abundance between pretreatment and on-treatment tissues, we utilized the compositional data analysis tool scCODA, which was applied to the scRNA-seq data. In the scCODA analysis, the reference for compositional changes was selected alternately, and the false discovery rate (FDR) was set at 0.1 for major cell lineages and 0.2 for subclusters.

## Single-cell TCR sequencing and clonotype analysis

TCR repertoire analysis was performed via the scReptero package<sup>76</sup> integrated with the scRNA-seq data. The raw TCR sequences were filtered to remove low-quality or non-productive chains. Contigs were combined across samples via combined TCR, retaining CDR3 amino acid sequences for clonotype calling (cloneCall = "aa"). TCR sequences were subsequently integrated into the Seurat object via combineExpression, preserving clone-cell associations.

Clonotypes were defined by unique CDR3 $\alpha$ -CDR3 $\beta$  pairs. The top 50 expanded clones were identified separately in the MPR and NMPR groups. Clone frequency was calculated as the proportion of cells belonging to each clonotype within response groups. To assess clonotype-subtype associations, we calculated the ratio of cells from each clone contributing to specific CD8+subsets. Wilcoxon rank-sum tests were used to compare clonotype distribution differences between the MPR and NMPR groups.

## CD8+ T-cell trajectory inference

To reconstruct the differentiation dynamics of CD8+T cell subsets, we performed RNA velocity<sup>77</sup> analysis followed by pseudotime trajectory modeling. Single-cell velocity vectors were estimated via scVelo (V.0.3.3) with default parameters, leveraging spliced/unspliced mRNA ratios to predict future transcriptional states with velocito (V.0.17.17). Transcriptional dynamics were modeled using the stochastic framework with full parameter estimation. The estimated velocities were then used to construct a velocity graph representing the transition probabilities among cells by function *scvelo.tl.velocity\_graph*. The velocity stream graph was embedded into the precomputed UMAP space by Seurat to visualize directionality. For pseudotime reconstruction, we applied Slingshot (V.2.6.0) to the UMAP embeddings.<sup>78</sup> The Tpx was designated the trajectory starting point on the basis of the RNA velocity results.

## CNV analysis

To identify tumor cells from epithelial populations, we performed CNV inference using endothelial cells as the reference group in scRNA-seq data. We reconstructed the CNV landscape of epithelial cells using infercnvpy (V.0.5.0) and selected endothelial cells as reference normal cells, with a 400-gene window size selected to mitigate noise while preserving large-scale chromosomal patterns. Following dimensional reduction and clustering based on CNV profiles, CNV scores were calculated using *infercnvpy.tl.cnv\_score* function. Given that all epithelial subpopulations exhibited significantly elevated CNV scores compared with normal cells, the entire epithelial compartment was classified as tumor cells.

## Gene set variation analysis

To assess pathway activity in individual cells and bulk RNA-seq samples, we applied GSVA using standard settings as

implemented in the GSVA R package (V.1.32.0), as previously described.<sup>79</sup> The gene set for the 50 hallmark pathways (h.all.v7.2.symbols.gmt) was downloaded from the Gene Set Enrichment Analysis (GSEA) website (<https://www.gsea-msigdb.org/gsea/index.jsp>). In addition, we used GSVA to evaluate the EP8 signature derived from our single-cell data. The differential activities of pathways between groups were calculated via the limma R package (V.3.42.2). Significantly perturbed pathways were identified with a Benjamini-Hochberg corrected p value of  $\leq 0.01$ .

## Survival analysis

Clinical outcome associations were evaluated via Kaplan-Meier survival curves and Cox proportional hazards models. Patients were stratified into high-risk and low-risk groups on the basis of the EP8 score. The signature was constructed by identifying overlapping DEGs between EP8 clusters ( $\log_2$  fold change  $>0.25$ , FDR  $<0.05$ ) and residual populations. GSVA was applied to bulk RNA-seq data from TCGA-CESC tumors (n=291) via the EP8 score gene set. Optimal score cutoffs for survival stratification were determined via maximally selected rank statistics via the survminer package. Survival differences between groups were assessed via log-rank tests, with HRs and 95% CIs calculated via univariate Cox regression. All analyses were adjusted for immortal time bias by excluding patients whose survival was less than 30 days. Statistical significance was defined as two-sided p  $<0.05$ .

## Transcription factor prediction

The activated regulons within distinct neutrophil subsets were analyzed via the single-cell regulatory network inference and clustering (pySCENIC) framework,<sup>80</sup> which uses the raw count matrix as input. Initially, the coexpression network was inferred via the runGenie3 algorithm, followed by the identification of regulons through RcisTarget. To quantify the activity of each regulon at the single-cell level, UCell scoring was subsequently employed.<sup>81</sup>

## Cell-cell interaction analysis

In this study, we employed two specialized software tools, CellChat and MultiNicheNet, to analyze cell-cell interactions within our single-cell dataset.

To analyze the interactions between different lineage subpopulations, we used CellChat. This software facilitates the inference and analysis of cell communication networks by incorporating known molecular interactions and signaling pathways. We used the raw count matrix as input and followed the default parameters for preprocessing, including normalization and scaling. The detection of signaling pathways was performed via the default method, and the communication probability was computed with the preset thresholds. CellChat provided insights into the signaling interactions and pathways active between distinct lineage subgroups, allowing us

to characterize the underlying cellular communication mechanisms.

Spatial cell–cell communication networks were inferred via CellChat on three human CC tissues with different pathological responses. Raw count matrices and spatial coordinates were processed via Seurat, with cell type labels assigned on the basis of CytoSPACE annotations. The spatial factors parameter was set to ratio=1 and tol=25. Ligand–receptor interactions from the Secreted Signaling subset of CellChatDB.human were analyzed.

Additionally, we applied MultiNicheNet to investigate interactions between major lineages. MultiNicheNet integrates multiple data sources to predict niche-specific ligand–receptor interactions and their downstream effects. We used the default settings for the prediction algorithms, which include the standard ligand–receptor database and predefined thresholds for interaction confidence. By leveraging this tool, we were able to map and quantify the communication between major lineage populations, offering a comprehensive view of the inter-lineage signaling landscape.

### Spatial transcriptome data processing

We processed the raw Stereo-seq data from our previously published study via the BGI Stereomics analytical pipeline. To characterize the spatial transcriptomic landscape of the tumor region comprehensively, we used a bin size of 100 (100×100 pixels, 49.72×49.72 μm) as the basic unit (spot) for downstream analyses. The preprocessed data were subsequently normalized via the SCTransform function in Seurat (V.4.0.4).

### Annotation of spots in stereo-seq slides

We annotated the spots on the basis of a reference-based integration workflow in Seurat. We then employed CytoSPACE (V.1.0.4) as an integration method, adhering to the documentation guidelines.<sup>82</sup> We created non-normalized count-based gene expression profiles and cell type label files from the scRNA-seq data, as well as non-normalized count-based gene expression profiles and spatial transcriptomics coordinate files from the Stereo-seq data. CytoSPACE was then executed using the recommended parameter settings. The single cells' assigned locations mapped to spatial transcriptomics spots were used to generate scatter plots, which facilitated direct comparisons between the different integration methods.

### Spatial distance analyses

Spatial proximity between epithelial and myeloid cells was quantified via a customized proximity index,<sup>53</sup> defined as the reciprocal of the shortest Euclidean distance between epithelial spots and myeloid subtype centroids in ST slides. Myeloid subsets, such as Macro\_IL1B, Macro\_CCL18, neutrophils, and LAMP3<sup>+</sup> dendritic cells, were annotated by transferring scRNA-seq cluster labels to myeloid spots in STs via the UCell scoring algorithm. For each epithelial spot, the proximity index was calculated for all myeloid subtypes and normalized across samples.

### RNA-seq library preparation and sequencing

Snap-frozen tumor biopsy tissues were homogenized, and total RNA was extracted via the AllPrep DNA/RNA Mini Kit (Qiagen). For library construction, 2 µg of high-quality RNA per sample was subjected to poly(A)+ mRNA enrichment via oligo(dT) magnetic beads. After fragmentation, first-strand cDNA was synthesized via random hexamer primers, followed by second-strand cDNA synthesis. The library was ready after end repair, A-tailing, adapter ligation, size selection, amplification, and purification. Paired-end sequencing (2×150 bp) was performed on a NovaSeq 6000 platform (Illumina), generating approximately 20 million reads per sample.

### RNA sequencing data processing

Following quality control, the raw sequencing reads were aligned to the *Mus musculus* reference genome (GRCm39) via the STAR aligner with default parameters. Transcript quantification was performed via featureCounts (Subread). Gene annotation was performed via the *Mus musculus* Ensembl Release 107 genome annotation file.

For functional enrichment analysis, count data were subjected to GSVA via the gsva R package (V.1.46.0) with the “GSVA” method. Gene sets were generated from scRNA-seq data, and human genes were mapped to mouse orthologs via the BioMart package.

### ChIP-seq data analysis

To investigate potential regulatory targets of XBP1, we analyzed ChIP-seq data generated from the HepG2 cell line. Filtered BAM files downloaded from the ENCODE database (accession number ENCSR988EVQ) were sorted and indexed via SAMtools and then converted to genome-wide coverage tracks (bigWig format) via bamCoverage from deepTools. Visualization was performed via the Integrative Genomics Viewer (V.2.7.2) by aligning the bigWig tracks to the GRCh38/hg38 reference genome. Input control data (ENCSR020QUJ) were loaded to baseline signal specificity. Track heights and color gradients were optimized for peak clarity.

### Cell lines

The human cervical cancer cell lines SiHa and ME180 and the mouse lung epithelial cell line TC-1 were purchased from the National Collection of Authenticated Cell Cultures. SiHa and TC-1 cells were cultured in DMEM (Gibco, cat No. C11995500BT), whereas ME180 cells were cultured in McCoy's 5A (Procell, cat No. PM150710) medium at 37°C under 5% CO<sub>2</sub>. The media were supplemented with 10% fetal bovine serum (VivaCell, cat No. C04001) and 1% penicillin and streptomycin (Gibco, cat No. 15140-122).

### Cell viability assessment

Cell viability was assessed using the Cell Counting Kit-8 (CCK-8; Dojindo, cat No. CK04-11). Briefly, cells were seeded in 96-well plates (2×10<sup>3</sup> cells per well) and incubated for 24 hours (37°C, 5% CO<sub>2</sub>). After treatment with

chemotherapy drugs for the indicated duration, 10 µL CCK-8 reagent was added to each well, followed by incubation at 37°C for 1–4 hours. Absorbance was measured at 450 nm using a Spark microplate reader (Tecan). IC<sub>50</sub> curve was calculated as previously described.<sup>83</sup>

### Syngeneic mouse tumor model

All animal procedures were approved by the Institutional Animal Care and Use Committees of Shanghai East Hospital (No. 2024-D322). 6-week-old female C57BL/6 mice (Cyagen Biosciences Suzhou) were used. Prior to the commencement of the experiment, the mice were subjected to a 1 week quarantine period. The animals were maintained in a controlled environment with a 12-hour light-dark cycle within the confines of the Laboratory Animal Care Centre at Tongji University, School of Medicine. The ambient temperature was maintained at 23±1°C, with relative humidity levels maintained between 50% and 60%.

For the syngeneic mouse tumor model, female C57BL/6 mice (5 weeks old) were subcutaneously inoculated with 5×10<sup>5</sup> TC-1 cells in 200 µL of phosphate-buffered saline in the right flank. The sample size of five mice per group was selected based on previous similar studies and in compliance with the ARRIVE (Animal Research: Reporting of In Vivo Experiments) guidelines to prioritize the minimization of animal use. Tumor growth was monitored every 48 hours starting at 48 hours post-inoculation. The mice were randomized into treatment groups when the tumors reached 100 mm<sup>3</sup>. Cisplatin (1.5 mg/kg, MCE, cat No. HY-17394), anti-PD-1 antibody (200 µg/mouse, MCE, cat No. HY-P99144), IgG isotype control (200 µg/mouse, MCE, cat No. HY-P990679) and the IRE1α inhibitor 4µ8C (10 mg/kg, MCE, cat No. HY-19707) were formulated in sterile saline, while paclitaxel (15 mg/kg, MCE, cat No. HY-B0015) was prepared in a vehicle containing 1% DMSO, 4% PEG300, 0.5% Tween-80, and 94.5% saline. Chemotherapeutic agents were administered intraperitoneally (i.p.) once weekly, whereas anti-PD-1 (i.p.) and 4µ8C (i.p.) were delivered two times per week. The mice were humanely euthanized by CO<sub>2</sub> asphyxiation when the tumors approached 1500 mm<sup>3</sup> or lost more than 20% of their body weight. Tumors were harvested for subsequent molecular and immunological analyses.

### Quantitative real-time PCR

Total RNA was extracted from cells or tissues via a Fast-Pure total RNA isolation kit (Vazyme, cat No. RC113-01) following the manufacturer's protocol. Reverse transcription was performed with 1 µg of total RNA with HiScript IV RT SuperMix for quantitative PCR (qPCR) (Vazyme, cat No. R423-01). qPCR amplification was carried out on a QuantStudio 6 Pro (Applied Biosystems) using ChamQ Universal SYBR qPCR Master Mix (Vazyme, cat No. Q711-02). The primer sequences for the target genes are listed in online supplemental table S5. Relative

mRNA expression was calculated via the 2<sup>-ΔΔCt</sup> method and normalized to that of ACTB.

### Western blotting

Protein lysates were extracted from cells or tissues via RIPA buffer (EpiZyme, cat No. PC101) supplemented with 1% protease inhibitor cocktail (MCE, cat No. HY-K0010) and phosphatase inhibitor cocktail (CST, cat No. 5870). Protein concentrations were quantified via a BCA assay (Beyotime, cat No. P0398M), and 20 µg of total protein was resolved on 10% SDS-PAGE gels (EpiZyme, cat No. PG112). Proteins were transferred to polyvinylidene fluoride (PVDF) membranes (Millipore, cat No. ISEQ00010) via a semidry transfer system (Bio-Rad) at 19 V for 2 hours. The membranes were blocked with 5% non-fat milk in Tris-buffered saline containing 0.1% Tween-20 (TBST) for 1 hour at room temperature and then incubated overnight at 4°C with the following primary antibodies: anti-SERPINA1 (Proteintech, 1:2000), anti-SAA1 (Abcam, 1:3000), anti-GDF15 (Proteintech, 1:2000), anti-ERN1 (Proteintech, 1:2000), anti-sXBP1 (Proteintech, 1:2000), and β-actin (Proteintech, 1:30000) as loading controls. The membranes were incubated with HRP-conjugated secondary antibodies (Proteintech, 1:2500) for 1 hour at room temperature after being washed three times with TBST. The protein bands were visualized via ECL Prime substrate (Cytiva) on a luminescent imaging system (Tanon, Chemi Dog 5200T).

### Multiplex immunohistochemistry

mIHC staining was performed according to the manufacturer's instructions and our previous study.<sup>40</sup> Briefly, 4 µm thick formalin-fixed paraffin-embedded sections were stained five times with primary antibodies for epithelial cells (anti-PanCK, 1:2000, CST), CD4 T cells (anti-CD4, 1:200, Abcam), CD8 T cells (anti-CD8, 1:1000, Proteintech), CD103 (Abcam, 1:100), and B cells (anti-CD20, Abcam), followed by tyramide signal amplification staining kits according to the manufacturer's instructions. The following primary antibodies were used for the myeloid panel: anti-PanCK (1:2000, CST), anti-CD14 (1:200, Gene Tech), anti-CD117 (1:200, Abcam), anti-CD66b (1:200, Abcam), anti-IL-1β (1:200, Abcam), anti-TGFBR2 (1:250, Starter), anti-GDF15 (1:300, Starter), and anti-CD11b (1:500, Starter). The slides were scanned via a ZEISS Axioscan 7 microscope slide scanner and analyzed via ZEN microscopy software (V.3.9).

### Statistical analysis

All the statistical analyses were conducted via R statistical software, V.4.3.0. The data were analyzed via the statistical methods outlined in the corresponding figure legends.

### Data and code availability

The datasets and computer code produced in this study are available for access in the following databases: scRNA-seq, scTCR-seq, and ST data for patients who underwent NACI treatment can be accessed from the Genome Sequence Archive (GSA) repository HRA007492<sup>84</sup> and



HRA012240<sup>85</sup> (<https://ngdc.cncb.ac.cn/gsa-human/>). Existing bulk RNA-seq datasets of CC (NACI cohort) and scRNA-seq data of primary CC tumors were downloaded from the Science Data Bank (<https://doi.org/10.57760/sciencedb.11624>). The TCGA-CESC cohorts were downloaded from UCSC Xena ([https://gdc.xenahubs.net/download/TCGA-CESC.htseq\\_counts.tsv.gz](https://gdc.xenahubs.net/download/TCGA-CESC.htseq_counts.tsv.gz)). The code used in this study is available from the corresponding authors on reasonable request.

#### Author affiliations

- <sup>1</sup>Department of Obstetrics and Gynecology, Shanghai East Hospital, School of Medicine, Tongji University, Shanghai, China
- <sup>2</sup>Department of Obstetrics and Gynecology, Tongji Hospital of Tongji Medical College of Huazhong University of Science and Technology, Wuhan, Hubei, China
- <sup>3</sup>State Key Laboratory of Cardiology and Research Center for Translational Medicine, Shanghai East Hospital, Tongji University School of Medicine, Shanghai, China
- <sup>4</sup>Department of Obstetrics and Gynecology, Queen Mary Hospital, Hong Kong, Hong Kong
- <sup>5</sup>Department of Pathology, Tongji University Affiliated East Hospital, Shanghai, Shanghai, China
- <sup>6</sup>Key Laboratory of Pathogen-Host Interaction (Tongji University), Ministry of Education, School of Medicine, Tongji University, Shanghai, China
- <sup>7</sup>Key Laboratory of Spine and Spinal Cord Injury Repair and Regeneration of Ministry of Education, Department of Orthopedics, Tongji Hospital, School of Life Science and Technology, Tongji University, Shanghai, Shanghai, China
- <sup>8</sup>Department of Obstetrics and Gynecology, Shanxi Bethune Hospital, Shanxi Academy of Medical Sciences, Third Hospital of Shanxi Medical University, TongjiShanxi Hospital, Taiyuan, Shanxi, China

**Contributors** The experiments were designed by FL and ZH. The experiment was carried out by GC, YZ, YG, MX, YR, YiW, YX, and JL. The bioinformatic analysis was performed by GC, YuW, and CW. The collection of samples was conducted by YuW and HZ. JG then proceeded to review the pathological results. The manuscript was authored by GC. The manuscript was revised by CW, KYT, and QZ. The manuscript was subject to a thorough editing and review process by all authors. FL is the guarantor of this work.

**Funding** This study was supported by the National Natural Science Foundation of China (No. 82472830, 82203512 and 82273091 to FL; 82372672 and 81974414 to ZH, and 82303180 to YZ), the Ministry of Science and Technology of the People's Republic of China (MOST, No. 2022YFA1106000 to CW), National Key R&D Program of China (No. 2024YFC2707400 to ZH), the Natural Science Foundation of Shanghai (No. 24ZR1492800 to CW), the Project of the Central Government Guiding Local in Shanxi Province (No. YDJSX2022B012 to ZH), Research and Innovation Team Project for Scientific Breakthroughs at Shanxi Bethune Hospital (No. 2024ZHANCHI08 to ZH), the East Hospital Clinical Research Foundation (No. DFLC2022028 to FL), and the Shanghai Pujian Programme (23PJ106 to YZ). Funders are not involved in the study design, the collection, analysis and interpretation of the data; the writing of the report, nor in the decision to submit the paper for publication.

**Competing interests** None declared.

**Patient consent for publication** Not applicable.

**Ethics approval** The use of biospecimens was approved by the Ethics Committee of Shanghai East Hospital with reference number EC.D. (BG).025.04.0. Participants gave informed consent to participate in the study before taking part.

**Provenance and peer review** Not commissioned; externally peer reviewed.

**Data availability statement** Data are available in a public, open access repository. The datasets and computer code produced in this study are available for access in the following databases: scRNA-seq, scTCR-seq, and ST data for patients who underwent NACI treatment can be accessed from the Genome Sequence Archive (GSA) repository HRA007492 and HRA012240 (<https://ngdc.cncb.ac.cn/gsa-human/>).

**Supplemental material** This content has been supplied by the author(s). It has not been vetted by BMJ Publishing Group Limited (BMJ) and may not have been peer-reviewed. Any opinions or recommendations discussed are solely those of the author(s) and are not endorsed by BMJ. BMJ disclaims all liability and

responsibility arising from any reliance placed on the content. Where the content includes any translated material, BMJ does not warrant the accuracy and reliability of the translations (including but not limited to local regulations, clinical guidelines, terminology, drug names and drug dosages), and is not responsible for any error and/or omissions arising from translation and adaptation or otherwise.

**Open access** This is an open access article distributed in accordance with the Creative Commons Attribution Non Commercial (CC BY-NC 4.0) license, which permits others to distribute, remix, adapt, build upon this work non-commercially, and license their derivative works on different terms, provided the original work is properly cited, appropriate credit is given, any changes made indicated, and the use is non-commercial. See <https://creativecommons.org/licenses/by-nc/4.0/>.

#### ORCID iDs

- Yuhan Wang <https://orcid.org/0000-0001-9134-0091>
- Chenfei Wang <https://orcid.org/0000-0001-7573-3768>
- Fang Li <https://orcid.org/0000-0003-0342-3941>

#### REFERENCES

- Colombo N, Dubot C, Lorusso D, et al. Pembrolizumab for Persistent, Recurrent, or Metastatic Cervical Cancer. *N Engl J Med* 2021;385:1856–67.
- Oaknin A, Gladieff L, Martínez-García J, et al. Atezolizumab plus bevacizumab and chemotherapy for metastatic, persistent, or recurrent cervical cancer (BEATcc): a randomised, open-label, phase 3 trial. *The Lancet* 2024;403:31–43.
- Tewari KS, Monk BJ, Vergote I, et al. Survival with Cemiplimab in Recurrent Cervical Cancer. *N Engl J Med* 2022;386:544–55.
- Lou H, Cai H, Huang X, et al. Cadonilimab Combined with Chemotherapy with or without Bevacizumab as First-Line Treatment in Recurrent or Metastatic Cervical Cancer (COMPASSION-13): A Phase 2 Study. *Clin Cancer Res* 2024;30:1501–8.
- Lorusso D, Xiang Y, Hasegawa K, et al. Pembrolizumab or placebo with chemoradiotherapy followed by pembrolizumab or placebo for newly diagnosed, high-risk, locally advanced cervical cancer (ENGOT-cx11/GOG-3047/KEYNOTE-A18): a randomised, double-blind, phase 3 clinical trial. *The Lancet* 2024;403:1341–50.
- Li K, Chen J, Hu Y, et al. Neoadjuvant chemotherapy plus camrelizumab for locally advanced cervical cancer (NACI study): a multicentre, single-arm, phase 2 trial. *Lancet Oncol* 2024;25:76–85.
- Pai JA, Hellmann MD, Sauter JL, et al. Lineage tracing reveals clonal progenitors and long-term persistence of tumor-specific T cells during immune checkpoint blockade. *Cancer Cell* 2023;41:776–90.
- Hu J, Zhang L, Xia H, et al. Tumor microenvironment remodeling after neoadjuvant immunotherapy in non-small cell lung cancer revealed by single-cell RNA sequencing. *Genome Med* 2023;15:14.
- Xu L, Saunders K, Huang S-P, et al. A comprehensive single-cell breast tumor atlas defines epithelial and immune heterogeneity and interactions predicting anti-PD-1 therapy response. *Cell Rep Med* 2024;5:101511.
- Liu B, Hu X, Feng K, et al. Temporal single-cell tracing reveals clonal revival and expansion of precursor exhausted T cells during anti-PD-1 therapy in lung cancer. *Nat Cancer* 2022;3:108–21.
- Chen Y, Wang D, Li Y, et al. Spatiotemporal single-cell analysis decodes cellular dynamics underlying different responses to immunotherapy in colorectal cancer. *Cancer Cell* 2024;42:1268–85.
- Li J, Wu C, Hu H, et al. Remodeling of the immune and stromal cell compartment by PD-1 blockade in mismatch repair-deficient colorectal cancer. *Cancer Cell* 2023;41:1152–69.
- Au L, Hatipoglu E, Robert de Massy M, et al. Determinants of anti-PD-1 response and resistance in clear cell renal cell carcinoma. *Cancer Cell* 2021;39:1497–518.
- Oliveira G, Egloff AM, Afeyan AB, et al. Preexisting tumor-resident T cells with cytotoxic potential associate with response to neoadjuvant anti-PD-1 in head and neck cancer. *Sci Immunol* 2023;8.
- Gebhardt T, Park SL, Parish IA. Stem-like exhausted and memory CD8+ T cells in cancer. *Nat Rev Cancer* 2023;23:780–98.
- Oliveira G, Wu CJ. Dynamics and specificities of T cells in cancer immunotherapy. *Nat Rev Cancer* 2023;23:295–316.
- Luo Y, Liang H. Single-cell dissection of tumor microenvironmental response and resistance to cancer therapy. *Trends Genet* 2023;39:758–72.
- Pu Y, Li L, Peng H, et al. Drug-tolerant persister cells in cancer: the cutting edges and future directions. *Nat Rev Clin Oncol* 2023;20:799–813.

- 19 Sehgal K, Portell A, Ivanova EV, et al. Dynamic single-cell RNA sequencing identifies immunotherapy persister cells following PD-1 blockade. *J Clin Invest* 2021;131:e135038.
- 20 Wang S, Zhu L, Li T, et al. Disruption of MerTK increases the efficacy of checkpoint inhibitor by enhancing ferroptosis and immune response in hepatocellular carcinoma. *Cell Rep Med* 2024;5:101415.
- 21 Lacher SB, Dörr J, de Almeida GP, et al. PGE2 limits effector expansion of tumour-infiltrating stem-like CD8+ T cells. *Nature New Biol* 2024;629:417–25.
- 22 Bell CR, Pelly VS, Moeini A, et al. Chemotherapy-induced COX-2 upregulation by cancer cells defines their inflammatory properties and limits the efficacy of chemoimmunotherapy combinations. *Nat Commun* 2022;13:2063.
- 23 Magen A, Hamon P, Fiaschi N, et al. Intratumoral dendritic cell-CD4<sup>+</sup> T helper cell niches enable CD8<sup>+</sup> T cell differentiation following PD-1 blockade in hepatocellular carcinoma. *Nat Med* 2023;29:1389–99.
- 24 Fridman WH, Meylan M, Petitprez F, et al. B cells and tertiary lymphoid structures as determinants of tumour immune contexture and clinical outcome. *Nat Rev Clin Oncol* 2022;19:441–57.
- 25 Wang XQ, Danenberg E, Huang C-S, et al. Spatial predictors of immunotherapy response in triple-negative breast cancer. *Nature New Biol* 2023;621:868–76.
- 26 Wei L-J, Fu J, Yang H-X, et al. Evaluation of pathological response to neoadjuvant chemotherapy in locally advanced cervical cancer. *J Transl Med* 2024;22:655.
- 27 Chandler C, Liu T, Buckanovich R, et al. The double edge sword of fibrosis in cancer. *Transl Res* 2019;209:55–67.
- 28 Escobar G, Tooley K, Oliveras J, et al. Tumor immunogenicity dictates reliance on TCF1 in CD8<sup>+</sup> T cells for response to immunotherapy. *Cancer Cell* 2023;41:1662–79.
- 29 Eberhardt CS, Kissick HT, Patel MR, et al. Functional HPV-specific PD-1<sup>+</sup> stem-like CD8 T cells in head and neck cancer. *Nature New Biol* 2021;597:279–84.
- 30 Zheng L, Qin S, Si W, et al. Pan-cancer single-cell landscape of tumor-infiltrating T cells. *Science* 2021;374:abe6474.
- 31 Ren X, Zhang L, Zhang Y, et al. Insights Gained from Single-Cell Analysis of Immune Cells in the Tumor Microenvironment. *Annu Rev Immunol* 2021;39:583–609.
- 32 Liu B, Zhang Y, Wang D, et al. Single-cell meta-analyses reveal responses of tumor-reactive CXCL13<sup>+</sup> T cells to immune-checkpoint blockade. *Nat Cancer* 2022;3:1123–36.
- 33 Chu Y, Dai E, Li Y, et al. Pan-cancer T cell atlas links a cellular stress response state to immunotherapy resistance. *Nat Med* 2023;29:1550–62.
- 34 Aoki H, Tsunoda M, Ogiwara H, et al. Clonal Spreading of Tumor-Infiltrating T Cells Underlies the Robust Antitumor Immune Responses. *Cancer Immunol Res* 2023;11:847–62.
- 35 Oliveira G, Stromhaug K, Klaeger S, et al. Phenotype, specificity and avidity of antitumour CD8+ T cells in melanoma. *Nature New Biol* 2021;596:119–25.
- 36 Montauti E, Oh DY, Fong L, CD4+ T cells in antitumor immunity. *Trends Cancer* 2024;10:969–85.
- 37 Brooks JF, Tan C, Mueller JL, et al. Negative feedback by NUR77/Nr4a1 restrains B cell clonal dominance during early T-dependent immune responses. *Cell Rep* 2021;36:109645.
- 38 Jin S, Guerrero-Juarez CF, Zhang L, et al. Inference and analysis of cell-cell communication using CellChat. *Nat Commun* 2021;12:1088.
- 39 Waldman AD, Fritz JM, Lenardo MJ. A guide to cancer immunotherapy: from T cell basic science to clinical practice. *Nat Rev Immunol* 2020;20:651–68.
- 40 Cao G, Yue J, Ruan Y, et al. Single-cell dissection of cervical cancer reveals key subsets of the tumor immune microenvironment. *EMBO J* 2023;42:e110757.
- 41 Zhang Y, Xu Z, Ye X, et al. Revealing a novel tumor immune escaping mechanism induced by macrophage-tumor fusion cells in HPV- cervical cancer through spatial SCRna analysis. *JCO* 2023;41:e17523.
- 42 Gast CE, Silk AD, Zarour L, et al. Cell fusion potentiates tumor heterogeneity and reveals circulating hybrid cells that correlate with stage and survival. *Sci Adv* 2018;4:eaat7828.
- 43 Kwon CH, Park HJ, Lee JR, et al. Serpin peptidase inhibitor clade A member 1 is a biomarker of poor prognosis in gastric cancer. *Br J Cancer* 2014;111:1993–2002.
- 44 Ma Y, Chen Y, Zhan L, et al. CEBPB-mediated upregulation of SERPINA1 promotes colorectal cancer progression by enhancing STAT3 signaling. *Cell Death Discov* 2024;10:219.
- 45 Chen X, Cubillos-Ruiz JR. Endoplasmic reticulum stress signals in the tumour and its microenvironment. *Nat Rev Cancer* 2021;21:71–88.
- 46 Zhang F, Zhou X, Zou H, et al. SAA1 is transcriptionally activated by STAT3 and accelerates renal interstitial fibrosis by inducing endoplasmic reticulum stress. *Exp Cell Res* 2021;408:112856.
- 47 Aguilera-Recarte D, Barroso E, Gumà A, et al. GDF15 mediates the metabolic effects of PPAR $\beta/\delta$  by activating AMPK. *Cell Rep* 2021;36:109501.
- 48 Cheng S, Li Z, Gao R, et al. A pan-cancer single-cell transcriptional atlas of tumor infiltrating myeloid cells. *Cell* 2021;184:792–809.
- 49 Somasundaram R, Connelly T, Choi R, et al. Tumor-infiltrating mast cells are associated with resistance to anti-PD-1 therapy. *Nat Commun* 2021;12:346.
- 50 Wu Y, Yi M, Niu M, et al. Myeloid-derived suppressor cells: an emerging target for anticancer immunotherapy. *Mol Cancer* 2022;21:184.
- 51 van Elsas MJ, Middelburg J, Labrie C, et al. Immunotherapy-activated T cells recruit and skew late-stage activated M1-like macrophages that are critical for therapeutic efficacy. *Cancer Cell* 2024;42:1032–50.
- 52 Browaeys R, Saelens W, Saeyns Y. NicheNet: modeling intercellular communication by linking ligands to target genes. *Nat Methods* 2020;17:159–62.
- 53 Barkley D, Moncada R, Pour M, et al. Cancer cell states recur across tumor types and form specific interactions with the tumor microenvironment. *Nat Genet* 2022;54:1192–201.
- 54 Shaul ME, Fridlander ZG. Tumour-associated neutrophils in patients with cancer. *Nat Rev Clin Oncol* 2019;16:601–20.
- 55 Massagué J, Sheppard D. TGF- $\beta$  signaling in health and disease. *Cell* 2023;186:4007–37.
- 56 Haake M, Haack B, Schäfer T, et al. Tumor-derived GDF-15 blocks LFA-1 dependent T cell recruitment and suppresses responses to anti-PD-1 treatment. *Nat Commun* 2023;14:4253.
- 57 Melero I, de Miguel Luken M, de Velasco G, et al. Neutralizing GDF-15 can overcome anti-PD-1 and anti-PD-L1 resistance in solid tumours. *Nature New Biol* 2025;637:1218–27.
- 58 Heinhuis KM, Ros W, Kok M, et al. Enhancing antitumor response by combining immune checkpoint inhibitors with chemotherapy in solid tumors. *Ann Oncol* 2019;30:219–35.
- 59 Galluzzi L, Buqué A, Kepp O, et al. Immunological Effects of Conventional Chemotherapy and Targeted Anticancer Agents. *Cancer Cell* 2015;28:690–714.
- 60 Zhang Y, Chen H, Mo H, et al. Single-cell analyses reveal key immune cell subsets associated with response to PD-L1 blockade in triple-negative breast cancer. *Cancer Cell* 2021;39:1578–93.
- 61 Nakayama K, Kataoka N. Regulation of Gene Expression under Hypoxic Conditions. *Int J Mol Sci* 2019;20:3278.
- 62 Palazón A, Aragónés J, Morales-Kastresana A, et al. Molecular pathways: hypoxia response in immune cells fighting or promoting cancer. *Clin Cancer Res* 2012;18:1207–13.
- 63 Hetz C, Zhang K, Kaufman RJ. Mechanisms, regulation and functions of the unfolded protein response. *Nat Rev Mol Cell Biol* 2020;21:421–38.
- 64 Salaroglio IC, Panada E, Moiso E, et al. PERK induces resistance to cell death elicited by endoplasmic reticulum stress and chemotherapy. *Mol Cancer* 2017;16:91.
- 65 Pommier A, Anaparthy N, Memos N, et al. Unresolved endoplasmic reticulum stress engenders immune-resistant, latent pancreatic cancer metastases. *Science* 2018;360.
- 66 Mandula JK, Chang S, Mohamed E, et al. Ablation of the endoplasmic reticulum stress kinase PERK induces paraptosis and type I interferon to promote anti-tumor T cell responses. *Cancer Cell* 2022;40:1145–60.
- 67 Rufo N, Garg AD, Agostinis P. The Unfolded Protein Response in Immunogenic Cell Death and Cancer Immunotherapy. *Trends Cancer* 2017;3:643–58.
- 68 Briukhovetska D, Dörr J, Endres S, et al. Interleukins in cancer: from biology to therapy. *Nat Rev Cancer* 2021;21:481–99.
- 69 Cubillos-Ruiz JR, Mohamed E, Rodriguez PC. Unfolding anti-tumor immunity: ER stress responses sculpt tolerogenic myeloid cells in cancer. *J Immunotherapy Cancer* 2017;5:5.
- 70 Li W, Pan L, Hong W, et al. A single-cell pan-cancer analysis to show the variability of tumor-infiltrating myeloid cells in immune checkpoint blockade. *Nat Commun* 2024;15:6142.
- 71 Ross SH, Cantrell DA. Signaling and Function of Interleukin-2 in T Lymphocytes. *Annu Rev Immunol* 2018;36:411–33.
- 72 Caronni N, La Terza F, Vittoria FM, et al. IL-1 $\beta$ + macrophages fuel pathogenic inflammation in pancreatic cancer. *Nature New Biol* 2023;623:415–22.
- 73 Doroshow DB, Bhalla S, Beasley MB, et al. PD-L1 as a biomarker of response to immune-checkpoint inhibitors. *Nat Rev Clin Oncol* 2021;18:345–62.



- 74 Monk BJ, Colombo N, Tewari KS, et al. First-Line Pembrolizumab + Chemotherapy Versus Placebo + Chemotherapy for Persistent, Recurrent, or Metastatic Cervical Cancer: Final Overall Survival Results of KEYNOTE-826. *J Clin Oncol* 2023;41:5505–11.
- 75 Wu X, Sun Y, Yang H, et al. Cadonilimab plus platinum-based chemotherapy with or without bevacizumab as first-line treatment for persistent, recurrent, or metastatic cervical cancer (COMPASSION-16): a randomised, double-blind, placebo-controlled phase 3 trial in China. *The Lancet* 2024;404:1668–76.
- 76 Borcherding N, Bormann NL, Kraus G. scRepertoire: An R-based toolkit for single-cell immune receptor analysis. *F1000Res* 2020;9:47.
- 77 La Manno G, Soldatov R, Zeisel A, et al. RNA velocity of single cells. *Nature New Biol* 2018;560:494–8.
- 78 Street K, Risso D, Fletcher RB, et al. Slingshot: cell lineage and pseudotime inference for single-cell transcriptomics. *BMC Genomics* 2018;19:477.
- 79 Xing X, Yang F, Huang Q, et al. Decoding the multicellular ecosystem of lung adenocarcinoma manifested as pulmonary subsolid nodules by single-cell RNA sequencing. *Sci Adv* 2021;7:eabd9738.
- 80 Aibar S, González-Blas CB, Moerman T, et al. SCENIC: single-cell regulatory network inference and clustering. *Nat Methods* 2017;14:1083–6.
- 81 Andreatta M, Carmona SJ. UCell: Robust and scalable single-cell gene signature scoring. *Comput Struct Biotechnol J* 2021;19:3796–8.
- 82 Vahid MR, Brown EL, Steen CB, et al. High-resolution alignment of single-cell and spatial transcriptomes with CytoSPACE. *Nat Biotechnol* 2023;41:1543–8.
- 83 Cao G, Li S, Shi H, et al. Schisandrin B attenuates renal fibrosis via miR-30e-mediated inhibition of EMT. *Toxicol Appl Pharmacol* 2019;385:114769.
- 84 Fang L. Single-cell RNA and TCR sequencing data from cervical cancer patients before and after neoadjuvant immunotherapy. Genome Sequence Archive; 2025. Available: <https://ngdc.cncb.ac.cn/gsa-human/browse/HRA007492>
- 85 Fang L. Spatial transcriptomes data from cervical cancer patients before and after neoadjuvant immunotherapy, HRA012240. Genome Sequence Archive; 2025. Available: <https://ngdc.cncb.ac.cn/gsa-human/browse/HRA012240>